

**FEMORAL FRACTURE RISK ASSESSMENT FOLLOWING DOUBLE-BUNDLE ACL  
RECONSTRUCTION**

by

**Madelyn Egan O'Farrell**

B.S. in Mechanical Engineering, University of Pittsburgh, 2006

Submitted to the Graduate Faculty of  
The School of Engineering in partial fulfillment  
of the requirements for the degree of  
Master of Science in Mechanical Engineering

University of Pittsburgh

2007

UNIVERSITY OF PITTSBURGH  
SCHOOL OF ENGINEERING

This thesis was presented

by

Madelyn Egan O'Farrell

It was defended on

November 12, 2007

and approved by

Dr. William S. Slaughter, Associate Professor, Department of Mechanical Engineering and  
Materials Science

Dr. Mark C. Miller, Associate Research Professor, Department of Mechanical Engineering  
and Materials Science

Dr. Patrick J. Smolinski, Associate Professor, Department of Mechanical Engineering and  
Materials Science, Thesis Advisor

Copyright © by Madelyn Egan O'Farrell

2007

# **FEMORAL FRACTURE RISK ASSESSMENT FOLLOWING DOUBLE-BUNDLE ACL RECONSTRUCTION**

Madelyn Egan O'Farrell, M.S.

University of Pittsburgh, 2007

The anterior cruciate ligament (ACL) is the major ligament in the knee and is often torn during athletic competition as well as every day activity. The ACL is made up of two functional bundles, which help to stabilize the knee. Until recently, ACL reconstruction only replaced one of these bundles; however, research shows that both bundles are needed to more fully restore normal knee anatomy. In order to replace both bundles, two tunnels must be drilled in the femur bone. With the drilling of two tunnels there are a few concerns, one of which is femur fracture. This study uses computational models as well as experimental testing to explore the different bone stresses in the femur caused by tunnel drilling during ACL reconstruction. Through the use of medical imaging and finite element analysis software, a computational model was developed having actual geometry and material properties of the human femur. The computational analysis was used to investigate the effect of the addition of a second tunnel, variations of tunnel placement, and tunnel diameter size on bone stress. Experimental data was gathered by attaching strain gage rosettes to human cadaver femurs and calculating the resulting principle strains. The results of both the experimental testing and computational analysis were compared and no significant difference was found between the two.

## TABLE OF CONTENTS

|   |           |
|---|-----------|
| <b>PREFACE.....</b>   | <b>XI</b> |
| <b>1.0 INTRODUCTION.....</b>                                  | <b>1</b>  |
| <b>1.1 ACL BACKGROUND.....</b>                                | <b>1</b>  |
| <b>1.2 ACL RECONSTRUCTION.....</b>                            | <b>2</b>  |
| <b>1.3 FEMUR FRACTURE RISK.....</b>                           | <b>4</b>  |
| <b>1.4 DOUBLE-BUNDLE ACL RECONSTRUCTION TECHNIQUE .....</b>   | <b>5</b>  |
| <b>2.0 COMPUTATIONAL ANALYSIS .....</b>                       | <b>8</b>  |
| <b>2.1 FINITE ELEMENT STRESS VALIDATION.....</b>              | <b>8</b>  |
| <b>2.2 SAWBONE FINITE ELEMENT MODEL .....</b>                 | <b>11</b> |
| <b>2.3 FINITE ELEMENT MODEL GENERATION FROM CT DATA .....</b> | <b>14</b> |
| <b>2.4 MODEL MANIPULATION .....</b>                           | <b>15</b> |
| <b>2.4.1 Tunnel Location .....</b>                            | <b>16</b> |
| <b>2.4.2 Tunnel Diameter .....</b>                            | <b>18</b> |
| <b>2.5 MESHING .....</b>                                      | <b>20</b> |
| <b>2.6 MATERIAL PROPERTIES.....</b>                           | <b>21</b> |
| <b>2.6.1 Sawbone Model Material Properties.....</b>           | <b>21</b> |
| <b>2.6.2 CT Scan Model Material Properties .....</b>          | <b>22</b> |
| <b>2.7 LOADING AND BOUNDARY CONDITIONS.....</b>               | <b>24</b> |

|                          |   |           |
|--------------------------|---|-----------|
| <b>2.8</b>               | <b>COMPUTATIONAL RESULTS.....</b>               | <b>25</b> |
| 2.8.1                    | Sawbone Model .....                             | 25        |
| 2.8.2                    | CT Scan Model.....                              | 28        |
| 2.8.3                    | Effect of Tunnel Position Variation.....        | 29        |
| 2.8.4                    | Effect of Uniform and Stepped Diameter .....    | 31        |
| <b>2.9</b>               | <b>DISCUSSION OF COMPUTATIONAL RESULTS.....</b> | <b>32</b> |
| 2.9.1                    | Sawbone vs. CT Scan Model .....                 | 33        |
| 2.9.2                    | Tunnel Location and Diameter .....              | 35        |
| <b>3.0</b>               | <b>EXPERIMENTAL TESTING .....</b>               | <b>36</b> |
| 3.1                      | TEST SPECIMENS.....                             | 36        |
| 3.2                      | TEST EQUIPMENT .....                            | 37        |
| 3.2.1                    | Compression Testing Machine.....                | 37        |
| 3.2.2                    | Strain Gage Attachment.....                     | 38        |
| 3.3                      | TESTING PROTOCOL.....                           | 41        |
| 3.4                      | EXPERIMENTAL TESTING RESULTS.....               | 42        |
| 3.4.1                    | Statistical Analysis .....                      | 43        |
| <b>4.0</b>               | <b>DISCUSSION .....</b>                         | <b>46</b> |
| 4.1                      | COMPUTATIONAL VS. EXPERIMENTAL .....            | 46        |
| <b>APPENDIX A .....</b>  |   | <b>48</b> |
| <b>APPENDIX B .....</b>  |   | <b>54</b> |
| <b>BIBLIOGRAPHY.....</b> |   | <b>62</b> |

## LIST OF TABLES

|   |    |
|---|----|
| Table 1. Clinical reports of femoral fracture following SB ACL reconstruction .....                                 | 4  |
| Table 2. AM and PL tunnel locations .....   | 18 |
| Table 3. Tunnel diameters and depths .....  | 20 |
| Table 4. R-squared value and slope for cadavers and computational models when plotted as micro-strain vs. load..... | 43 |
| Table 5. Average and standard deviation for r-squared value and slope of cadaver results.....                       | 43 |

## LIST OF FIGURES

|  |    |
|--|----|
| Figure 1. ACL anatomy .....  | 2  |
| Figure 2. Intact (A), single-bundle (B), double-bundle (C).....                                | 3  |
| Figure 3. Anatomical footprint at 0° (a) and 90° (b) flexion.....                              | 3  |
| Figure 4. The three portals and incision line used when performing DB ACL reconstruction ..... | 6  |
| Figure 5. Schematic of tunnel placement in DB ACL reconstruction .....                         | 6  |
| Figure 6. Excised AM and PL bundle lengths .....   | 7  |
| Figure 7. Cylinder mesh.....   | 9  |
| Figure 8. Stress contour plot .....  | 10 |
| Figure 9. Sawbone model AM tunnel geometry with o'clock positions .....                        | 13 |
| Figure 10. Sawbone model PL tunnel geometry with o'clock positions .....                       | 13 |
| Figure 11. CT scan model.....  | 15 |
| Figure 12. Two x-rays showing varying tunnel placement.....                                    | 16 |
| Figure 13. Exit regions for AM and PL tunnels.....   | 17 |
| Figure 14. Endo-button fixation device, stepped diameter .....                                 | 19 |
| Figure 15. Refined mesh at AM tunnel exit.....   | 21 |
| Figure 16. DIACOM image and approximate pixels.....  | 22 |
| Figure 17. Meshed femur, loaded and constrained.....   | 25 |

|  |    |
|--|----|
| Figure 18. Location of highest stress concentration for one tunnel case .....  | 26 |
| Figure 19. SCF for double, single, and intact cases vs. distance along AM tunnel axis for the sawbone model.....                                     | 27 |
| Figure 20. SCF for double, single, and intact cases vs. distance along PL tunnel axis for the sawbone model.....                                     | 27 |
| Figure 21. SCF for double, single, and intact cases vs. distance along AM tunnel axis for the CT scan model .....                                    | 28 |
| Figure 22. SCF for double, single, and intact cases vs. distance along PL tunnel axis for the CT scan model .....                                    | 29 |
| Figure 23. Max stress in AM tunnel models for AM and PL tunnel exit regions .....  | 30 |
| Figure 24. Max stress in PL tunnel models for AM and PL tunnel exit regions .....  | 30 |
| Figure 25. Max stress in AM and PL tunnel diameter models, stepped-S or uniform-U followed by AM/PL diameter .....                                   | 32 |
| Figure 26. Lateral view of models depicting difference in tunnel placement and exit diameter used in CT scan (left) and sawbone (right) models ..... | 34 |
| Figure 27. Test equipment set-up.....  | 37 |
| Figure 28. Composite sawbones .....  | 39 |
| Figure 29. Strain gage attached to potted sawbone.....   | 40 |
| Figure 30. Cadaver with mounted gage, set up for testing .....   | 41 |
| Figure 31. Chart showing strain ( $\mu\epsilon$ ) at 1000 N for sawbone model (SB), CT scan model (CT) and cadavers 1-11 (C1-C11).....               | 45 |
| Figure 32. Chart showing strain ( $\mu\epsilon$ ) at 100 N for all models and cadavers.....  | 55 |
| Figure 33. Chart showing strain ( $\mu\epsilon$ ) at 200 N for all models and cadavers.....  | 55 |
| Figure 34. Chart showing strain ( $\mu\epsilon$ ) at 300 N for all models and cadavers.....  | 56 |
| Figure 35. Chart showing strain ( $\mu\epsilon$ ) at 400 N for all models and cadavers.....  | 56 |
| Figure 36. Chart showing strain ( $\mu\epsilon$ ) at 500 N for all models and cadavers.....  | 57 |
| Figure 37. Chart showing strain ( $\mu\epsilon$ ) at 600 N for all models and cadavers.....  | 57 |

|  |    |
|--|----|
| Figure 38. Chart showing strain ( $\mu\epsilon$ ) at 700 N for all models and cadavers.....  | 58 |
| Figure 39. Chart showing strain ( $\mu\epsilon$ ) at 800 N for all models and cadavers.....  | 58 |
| Figure 40. Chart showing strain ( $\mu\epsilon$ ) at 900 N for all models and cadavers.....  | 59 |
| Figure 41. Chart showing strain ( $\mu\epsilon$ ) at 1000 N for all models and cadavers..... | 59 |
| Figure 42. Chart showing strain ( $\mu\epsilon$ ) at 1100 N for all models and cadavers..... | 60 |
| Figure 43. Chart showing strain ( $\mu\epsilon$ ) at 1200 N for all models and cadavers..... | 60 |
| Figure 44. Chart showing strain ( $\mu\epsilon$ ) at 1300 N for all models and cadavers..... | 61 |

## **PREFACE**

I would first like to say thank you to Dr. Freddie H. Fu, one of the pioneers of double-bundle anterior cruciate ligament reconstruction and the driving force behind many projects relating to this surgery. I would like to acknowledge the help of Dr. Lopes, Dr. Ferretti, and Dr. Yoo who volunteered their time to contribute to the medical aspect of this research project. For the computer modeling portion of the project, I would like to thank Kevin Bell and Gulshan Sharma for their help and guidance. To my advisor, Dr. Smolinski, thank you for giving me the opportunity to begin research as an undergraduate and introducing me to an area of engineering that I am most passionate about. Lastly, I would like to thank my family and especially my parents and husband for their constant love, support, and encouragement.

## **1.0 INTRODUCTION**

### **1.1 ACL BACKGROUND**

The anterior cruciate ligament (ACL) is the main ligament in the knee and is often torn during athletic competition as well as every day activities. As a result, ACL reconstruction is a common procedure with about 100,000 surgeries performed each year in the United States alone (Boden 2000). Research has shown that the ACL is made up of two functional bundles: the anterior medial (AM) bundle, and the posterior lateral (PL) bundle (Figure 1). The AM bundle largely controls translational movement, while the PL bundle is primarily responsible for rotational movement in the knee (Zelle 2006). Both bundles work together to provide overall knee stability and effective joint mobility.

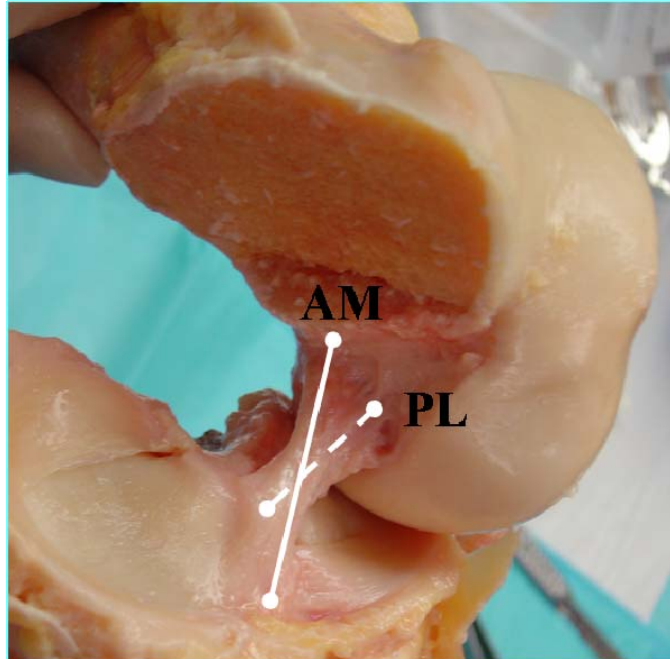


**Figure 1.** ACL anatomy

## **1.2 ACL RECONSTRUCTION**

Until recently, only single-bundle (SB) ACL reconstructions were performed, which replace the total ACL with only one bundle. However, by replacing both the AM and PL bundles, surgeons are better able to restore normal, intact knee kinematics. This anatomical, or double-bundle (DB), reconstruction replaces both bundles of the ACL and allows for a better restoration of both translation and rotation in the knee (Zelle 2006, Yagi 2002). Replacing both bundles may also prevent the future development of osteoarthritis in the knee. Osteoarthritis, also called degenerative arthritis, is an irreversible and painful disease in the cartilage lining the joint, with no current cure only methods and theories of prevention (Clatworthy 1999).

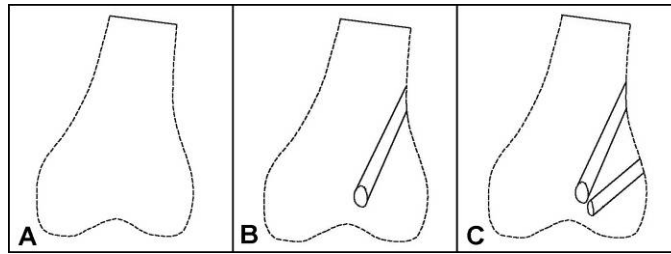


**Figure 2.** Intact (A), single-bundle (B), double-bundle (C)

DB ACL reconstruction uses two grafts to replace both the AM and PL bundles of the ACL. This requires that two tunnels be drilled in the femur, as opposed to one for the SB surgery (Figure 2). By using two grafts, surgeons are better able to restore both major functions of the ACL. They also use the anatomical femoral insertion site, or anatomical footprint, as a guide when placing the tunnels for graft insertion. When performing a SB reconstruction, the tunnel placement is ambiguous, leaving room for error. However, with the DB reconstruction, each tunnel has a specified position on the footprint and there is less room for error (Zelle 2006). Figure 3 shows the location of the anatomical footprint on the femur, and the placement of the AM and PL tunnels within the footprint.

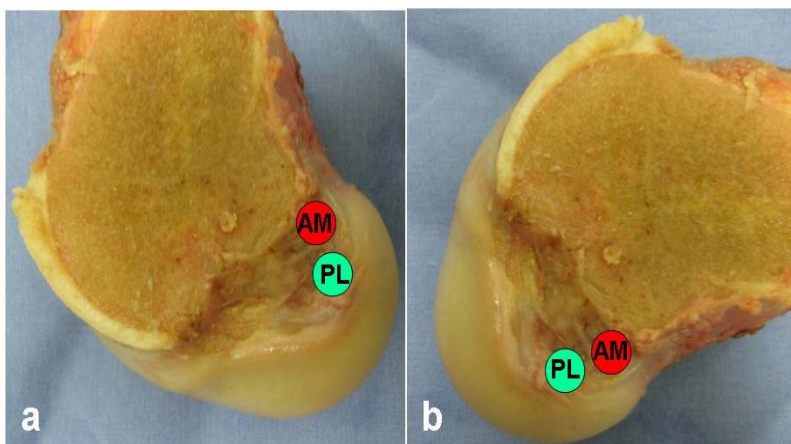


**Figure 3.** Anatomical footprint at 0° (a) and 90° (b) flexion

### 1.3 FEMUR FRACTURE RISK

There are concerns with drilling multiple tunnels in the bone. One of these concerns is whether there will be an increase in the risk of femur fracture (Harner 2004). Femur fracture is a devastating complication and has been reported in isolated cases for a SB reconstruction (Table 1). Thus, it becomes important to assess whether or not the risk of fracture increases with the addition of a second tunnel.

**Table 1.** Clinical reports of femoral fracture following SB ACL reconstruction

| <b>Author (year)</b> | <b>Fracture</b>   | <b>Stress Riser</b>                | <b>Time Post-Surger</b> | <b>Graft</b>          |
|----------------------|---|------------------------------------|-------------------------|-----------------------|
| Noah (1992)          | Femoral fracture at level of iliotibial band screw  | Iliotiabial band screw             | 6 mos                   | Patellar tendon graft |
| Ternes (1993)        | Supracondular femoral fracture involving diaphyseal hole  | Large femoral diaphyseal hole      | 8 wks                   | GORE-TEX              |
| Berg (1994)          | Displaced coronal fracture of posterior half of lateral femoral condyle                               | Femoral screw post                 | 2 mos                   | Patellar tendon graft |
| Wiener (1996)        | Oblique femoral fracture at junction of distal shaft and metaphysis through the tunnel                | Multiple passes of trocar pin      | 7 mos                   | Patellar tendon graft |
| Manktelow (1998)     | Displaced fracture of lateral femoral condyle through extra-articular staple                          | Extra-articular tenodesis (staple) | 24 mos                  | Hamstring graft       |
| Radler (2000)        | Supercondular & diacondular femoral fracture through screw hole of ligament augmentation device (LAD) | LAD                                | 25 mos                  | Marshall technique    |
| Wilson (2004)        | Intra-articular fracture of lateral femoral condyle through the femoral tunnel                        | Femoral tunnel                     | 9 mos                   | Patellar tendon graft |

## **1.4 DOUBLE-BUNDLE ACL RECONSTRUCTION TECHNIQUE**

There are various methods of restoring the ACL and performing a DB surgery. The DB reconstruction is a lengthy surgery that requires skill and precision. One of the pioneers of this surgery is Dr. Freddie H. Fu, Chairman of the Orthopaedic Department at UPMC. The techniques used in this study will be based largely on observing his surgeries.

When performing the DB surgery, three portals are created for viewing and use of instrumentation during surgery (Cohen 2007). The portals are made by making a small incision near the knee joint. The high portal (anterolateral portal) is used for viewing and placed on the lateral side. The central portal (anteromedial portal) is created as both a viewing and working portal for marking of the AM and PL insertion sites. It is placed near the center of the knee. The accessory portal (accessory anteromedial portal) is the working portal for the PL tunnel placement, and is placed on the medial side of the knee. To drill the AM tunnel, the tibial incision line is used and the tunnel is drilled trans-tibially, or through the tibia tunnel. A schematic of the portals is shown in Figure 4 (Cohen 2007), and Figure 5 shows the tibia and femur after the tunnels have been drilled.

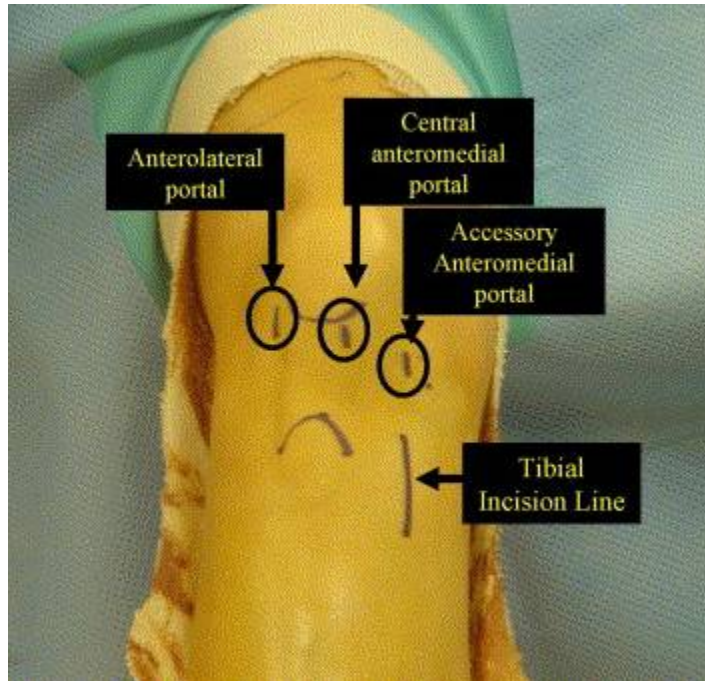


**Figure 4.** The three portals and incision line used when performing DB ACL reconstruction



**Figure 5.** Schematic of tunnel placement in DB ACL reconstruction

After the tunnels are drilled, the bundles are inserted. Typically, the AM and PL bundles are made up of allograft tissue (cadaver tissue), which may include Hamstring, Tibialis, and Achilles tendons (Zantop 2007). The native AM bundle ranges from 6-8 mm in diameter and 28-

38 mm in length, while the native PL bundle is 5-7 mm in diameter and has a mean length of 17.8 mm (Zantop 2006, Buoncristiani 2006). Figure 5 shows a side by side view of the AM and PL bundles (Zantop 2006).

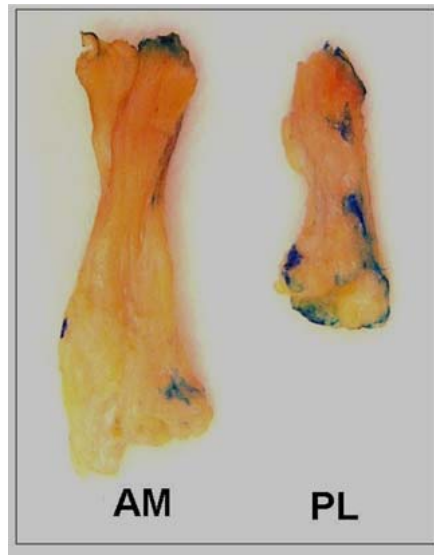


**Figure 6.** Excised AM and PL bundle lengths

## **2.0 COMPUTATIONAL ANALYSIS**

The computational analysis was conducted using finite element analysis (FEA), which obtains a solution to a complex problem by subdividing it into a collection of smaller, simpler problems that can be solved using numerical techniques (Cowin 1989). The complex problem in this case was the femur bone geometry. FEA offers an approximate solution to this problem through the use of computer software for computations. The software uses elements of a known geometry and a given edge size to make up the geometry of the unknown object. Boundary conditions are then applied after which the software can solve the model and give results for stress and strain of each element as well as each node.

### **2.1 FINITE ELEMENT STRESS VALIDATION**

The FEA software ANSYS (version 10.0, ANSYS inc., Canonsburg, PA), was used in this study to perform a stress analysis on a three-dimensional model of the femur. To validate the results of this software, an object of known geometry was modeled and tested and the results were compared to an analytical solution for that same geometry. A cylinder was used as a simplified model of the femur shaft (Figure 7). The diameter of the cylinder was 31 mm, which is similar to the diameter of the femoral shaft. An intact cylinder was tested in compression with one end constrained in all degrees of freedom. Then, a hole was cut through the center of the cylinder

with a diameter of 7 mm, which is similar to the size of the tunnels drilled in the femur. The cylinder was then tested again to determine a stress concentration factor (SCF) at the hole, or the ratio of the stress in the cylinder with the hole to the stress in the cylinder without the hole. The length of the cylinder was chosen to be 100 mm so that the applied loading was far enough away from the location of the hole so as not to have an effect on the stress at the hole (St. Venant's Principle). Both intact and hole models were meshed with approximately 60,000 tetrahedral elements, which is the same type and about the same number of elements used to mesh the femur bone (see Section 2.5).

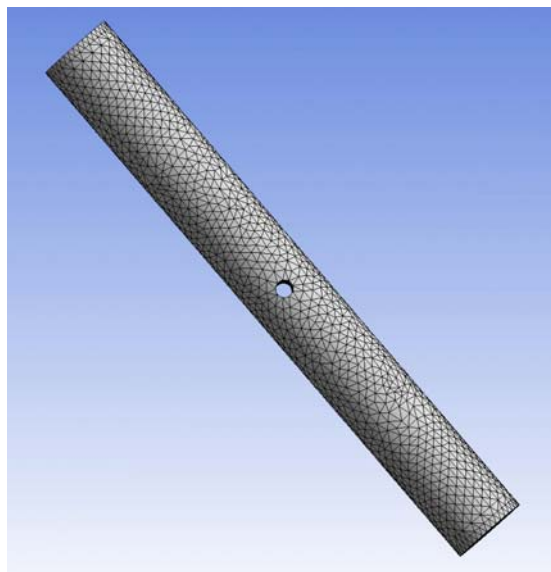


**Figure 7.** Cylinder mesh

A Young's Modulus of cortical bone (see Section 2.6) was used and Poisson's ratio was set equal to zero. This was done because the analytical solution used to compare results, provides stress concentration factors in one direction only and depends on geometry not material properties (Pilkey 1997). In the intact cylinder, the stress was shown to be uniform, in the

direction of the applied load, and equal to the applied pressure, as expected, and agreed with the analytical solution.

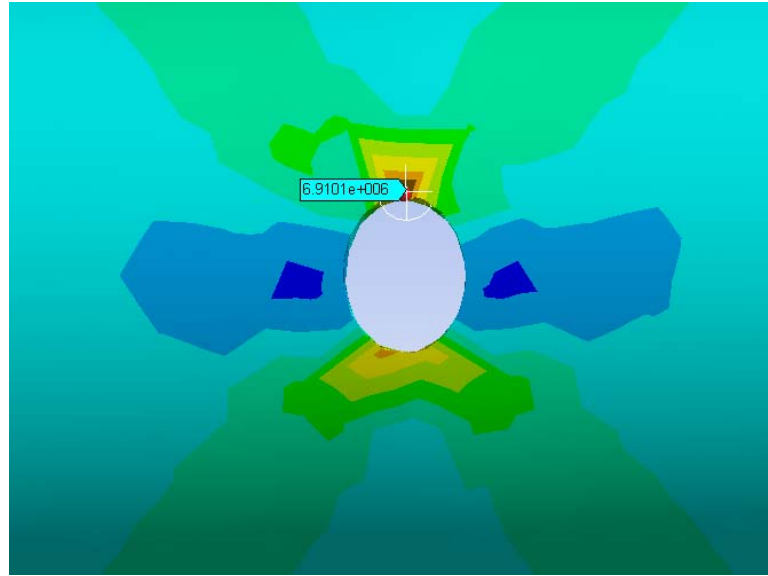


**Figure 8.** Stress contour plot

Figure 8 shows the stress contour plot at the hole. As shown in the figure, the contour plot is not symmetric in both directions. This is most likely due to the mesh and element edge size. By taking the max stress at the hole and the uniform stress from the intact cylinder, a SCF can be determined using the following equation.

$$SCF = \frac{\sigma_{\text{hole}}}{\sigma_{\text{intact}}} = \frac{6.89MPa}{2.65MPa} = 2.60 \quad (1)$$

The analytical solution of stress concentration at the hole for a cylinder was obtained from charts. These analytical stress charts can be found for a variety of geometries; however, they only give results for a single material object, not a composite (Pilkey 1997). Although bone is a composite material, a single material cylinder was modeled here to compare the

computational results from the finite element software directly to the analytical results from the charts (Pilkey 1997). The factor used to determine the analytical SCF from the charts is the diameter ratio of the hole and cylinder (Equation 2).

$$\frac{d}{D} = \frac{7 \text{ mm}}{31 \text{ mm}} = 0.226 \quad (2)$$

This ratio yields an analytical SCF of 2.75, which differs only slightly from the computational SCF of 2.60 (5.5% difference). This was considered satisfactory, and ANSYS was then used to model the femur bone, a more complex geometry.

## **2.2 SAWBONE FINITE ELEMENT MODEL**

The first model created to represent the femur geometry was taken from composite sawbone models (Sawbones, Pacific Research Labs, Vashon Island, WA, Viceconti 1996), which are available on the Internet at the Biomechanics European Laboratory (BEL) Repository website (BEL R 2005). This solid model of the femur, called The Standardized Femur, is made up of two parts, cortical (hard outer bone shell) and cancellous (soft inner bone tissue), and simulates the bony geometry of the knee. The model was cut mid-shaft so that only the distal portion of the femur was used. This was done in order to minimize the number of elements used in the meshing process, while still obtaining a sufficient element size and refinement (see Section 2.5 for meshing details).

The model was loaded into SolidWorks (SolidWorks Corporation, 2006 version) in order to create the tunnels used in the surgery. The tunnels were placed according to methods found in literature (Christel 2005, Zantop 2005). These methods use the two-dimensional o'clock position to place the tunnels. Though other methods of tunnel placement have evolved to include specific anatomy of the bone when placing the tunnels (Algietti 2005), the methods used here are based on geometry for ease in tunnel placement within SolidWorks. The AM tunnel was placed 5 mm from the posterior border of the lateral femoral condyle in the 11:00 position. The PL tunnel was placed at the 9:30 position. After tunnel placement, only a thin solid ridge existed between the AM and PL tunnel entrances.

Figures 9 and 10 show the geometry references used to place the AM and PL tunnels respectively. The long axis of the femur is the 12:00 position, the AM axis falls on the 11:00 position, and the PL axis falls on the 9:30 position. The AM work plane, shown in Figure 9, was created perpendicular to the AM tunnel axis and then tilted 70 degrees to simulate the knee bending 70 degrees of flexion (the approximate angle used in surgery when drilling the AM tunnel). A sketch of the AM tunnel was then made on this plane, centered at the coordinate system shown in Figure 9, and used to create the tunnel along the AM axis. The PL work plane, shown in Figure 10, was created perpendicular to the PL tunnel axis, and tilted 15 degrees to simulate the knee bending to 15 degrees of flexion (the angle used in surgery to drill the PL tunnel). Similar to the AM tunnel, the PL tunnel sketch was made on this plane, and the PL axis was used to place the tunnel centered at the coordinate system shown in Figure 10. Each tunnel exits the femoral shaft on the lateral side of the femur along the respective tunnel axis.

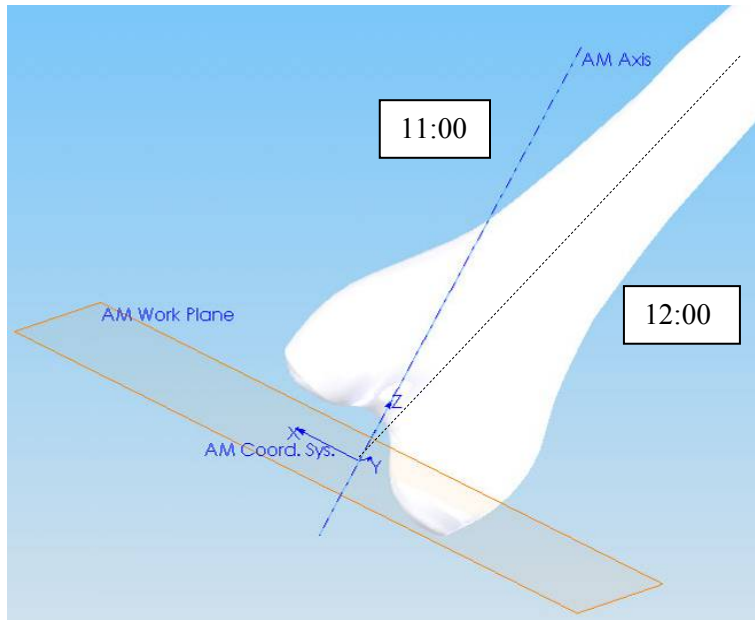


**Figure 9.** Sawbone model AM tunnel geometry with o'clock positions

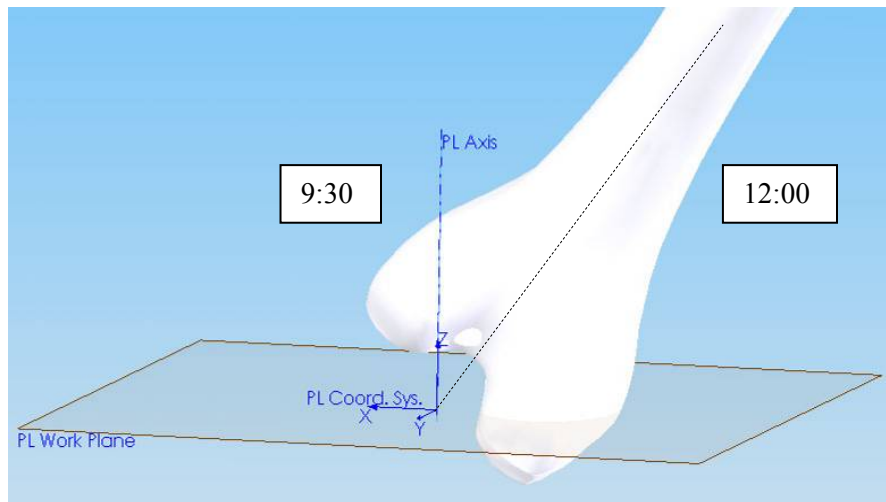


**Figure 10.** Sawbone model PL tunnel geometry with o'clock positions

According to literature, the native AM bundle diameter ranges from 6 to 8 mm, and the PL bundle diameter ranges from 5 to 7 mm (Christel 2005, Algietti 2005). When creating the tunnel size in the sawbone model, an average was used. Thus, the diameter of the AM tunnel was a constant 7 mm, and the diameter of the PL tunnel was a constant 6 mm. Three different models

were tested: intact, single-bundle, and double-bundle, and the results of each compared (see Sections 2.7, 2.8 for boundary conditions, solution, and results).

### **2.3 FINITE ELEMENT MODEL GENERATION FROM CT DATA**

Another form of model construction was used to obtain the actual geometry and material properties of the human femur bone. To do this, images were gathered from a computed tomography (CT) scan, which was previously taken of a knee. A CT scan divides the femur into slices, and captures a digital gray scale image of each slice. These slices are stored as DIACOM files, which stands for digital imaging and communications in medicine. In this case, the CT scan was taken axially along the femur and the slices were one millimeter apart. The files were then used to generate a more anatomical femur model, through the use of various software programs.

First, a program called AMIRA (AMIRA International, version 3.0), which is an advanced 3-D visualization and volume modeling software, was used to interpret the DIACOM files from the CT scan into a surface model of the femur. This was done by selecting the femur bone on each slice and specifying an appropriate threshold value for the scale of gray which corresponds to the density. Once all femur bone was selected, an outline of each slice was generated and compiled to form a 3-D surface model of the femur.

After using AMIRA, the 3D image contained sharp corners and uneven surfaces due to the slice spacing of the CT scan. Using a modeling program called Rapidform (Rapidform Incorporated, 2006 version), the surface of the model was smoothed and any overlapping surfaces or holes were repaired. Next, SolidWorks was used for physical manipulation of the

model (i.e. tunnel placement), and the model was cut mid shaft so that only the distal end of the femur was used for meshing, just as the sawbone model was cut. Figure 11 shows the finished model. Finally, the model was transported into ANSYS for meshing, assignment of material properties, boundary conditions, and solution to obtain values of stress.



**Figure 11.** CT scan model

## **2.4 MODEL MANIPULATION**

Two tunnels were placed in the CT scan model using SolidWorks, before it was transported into ANSYS. For the first case of the CT scan model tested in ANSYS, the same tunnel placement used in the sawbone model was used in order to make a direct comparison between resulting stresses in both models.

### 2.4.1 Tunnel Location

After this first case, several other cases of the CT scan model, each with a different tunnel placement, were created to analyze the effect of tunnel placement on femur fracture following the DB ACL reconstruction. The DB reconstruction is a new technique that is constantly changing and improving. Thus, the tunnel placement has changed in order to improve post-operative results. The sawbone model was the first model created and thus, the tunnel placement has already shifted since the time the tunnels were placed in that model.

In order to determine a “standard” tunnel placement for the new cases, ten recent x-rays showing anterior and lateral views of the femur after the surgery were used. Dr. Fu performed all ten of the reconstructions. Figure 12 contains two different x-rays taken after DB ACL reconstructions. These x-rays show how the tunnel placement can vary, even though the same surgeon performed both reconstructions.



**Figure 12.** Two x-rays showing varying tunnel placement

Angle measurements were taken of the tunnels, from the vertical, on both views and an average tunnel placement was determined. Each tunnel had the same entrance point, because the surgeon uses the same bony landmarks to place the tunnel entrance. Variation occurs because the degree of flexion at which the knee is held is not always accurate. Also, the axial rotation of the tibia with respect to the femur during tunnel drilling is not constant from patient to patient. These two factors greatly contribute to the varying tunnel exit locations. Thus, angles at which the tunnels were placed in the model were varied by adding five degrees to the standard angle in the following directions: anterior, posterior, lateral, medial (Figure 13). The AM and PL tunnel exit regions shown in Figure 13 contain all possible exits for each tunnel and will later be used to analyze the stress results.

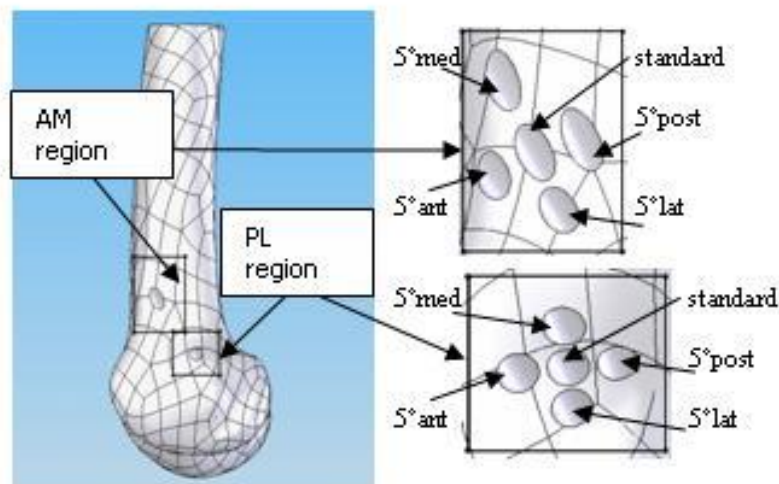


**Figure 13.** Exit regions for AM and PL tunnels

Multiple variations from this initial tunnel position were performed to analyze the effect of tunnel placement on bone stress and in turn, femur fracture. Table 2 shows the initial (standard) tunnel placement (right knee) and the subsequent variations. Only one angle was

varied at a time, keeping the remaining angles constant and consistent with the standard model. The angle varied is in bold face within the table.

**Table 2. AM and PL tunnel locations**

| <b>Case</b>    | <b>Tunnel</b> | <b>Axial View (deg)</b> | <b>Lateral View (deg)</b> |
|----------------|---------------|-------------------------|---------------------------|
| Standard (# 0) | AM            | 22                      | 29                        |
|                | PL            | 42                      | 20                        |
| AM 1           | AM            | <b>27</b>               | 29                        |
|                | PL            | 42                      | 20                        |
| AM 2           | AM            | <b>17</b>               | 29                        |
|                | PL            | 42                      | 20                        |
| AM 3           | AM            | 22                      | <b>34</b>                 |
|                | PL            | 42                      | 20                        |
| AM 4           | AM            | 22                      | <b>24</b>                 |
|                | PL            | 42                      | 20                        |
| PL 1           | AM            | 22                      | 29                        |
|                | PL            | <b>47</b>               | 20                        |
| PL 2           | AM            | 22                      | 29                        |
|                | PL            | <b>37</b>               | 20                        |
| PL 3           | AM            | 22                      | 29                        |
|                | PL            | 42                      | <b>25</b>                 |
| PL 4           | AM            | 22                      | 29                        |
|                | PL            | 42                      | <b>15</b>                 |

## **2.4.2 Tunnel Diameter**

Another variable that may affect stresses within the femur bone is the tunnel size used for graft placement. In order to analyze tunnel size, several more cases of the CT scan model were manipulated to show the effects of different diameters on femur fracture following DB ACL reconstruction. Stepped tunnel diameters result from the fixation device and graft size used during surgery. The effects of tunnel diameter were analyzed in a similar fashion as tunnel location.

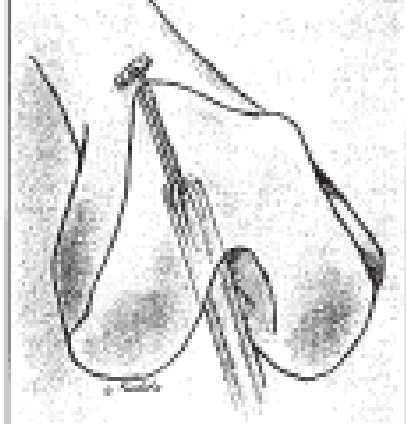


**Figure 14.** Endo-Button fixation device, stepped diameter

A range of generally accepted diameters were taken from literature and verified with several UPMC surgeons (Algietti 2005, Christel 2005). The smaller tunnel diameter, which begins at the depth specified in Table 3, is a constant 4.5 mm regardless of the depth or large diameter of the tunnels. The stepped tunnel diameter corresponds to an Endo-Button type fixation (Figure 14, Milano 2006), while the uniform diameter is used with an interference screw. Table 3 shows the variations in tunnel diameter and whether they are uniform or stepped. After varying the diameter size in SolidWorks, several finite element cases of the CT scan model were created for each variation. These models were meshed, loaded, and solved in ANSYS as will be described in the next sections.

**Table 3. Tunnel diameters and depths**

| <b>Case</b> | <b>Tunnel</b> | <b>Diameter (mm)</b> | <b>Depth (mm)</b> |
|-------------|---------------|----------------------|-------------------|
| S 7/6       | AM            | 7                    | 30                |
|             | PL            | 6                    | 25                |
| U 7/6       | AM            | 7                    | through           |
|             | PL            | 6                    | through           |
| S 8/7       | AM            | 8                    | 30                |
|             | PL            | 7                    | 25                |
| U 8/7       | AM            | 8                    | through           |
|             | PL            | 7                    | through           |

## **2.5 MESHING**

Each manipulated tunnel and diameter variation case of the CT scan model as well as the sawbone model were meshed, loaded, and solved individually. They were all meshed with 10-node tetrahedral elements, which have been shown to be the most effective element choice when meshing irregular geometries (Viceconti 1998). In order to reduce the number of elements used in the model, only the distal half of the femur was used. This is a reasonable simplification because the point of interest is the knee, or the most distal part of the femur.

An element edge length of 20 mm was specified for the entire model, and the areas around and inside the tunnels were selected and given a refined element edge length of 2 mm. This was done to eliminate sharp edges that may cause a false stress riser at the tunnels, and would ultimately affect the results. Refinement at the tunnels changed stress results by about 12% from the larger element edge length of 20 mm. When an edge length less than 2 mm was used, there was only a 1% change in stress; thus, 2 mm was determined appropriate for the refinement element edge length. After refinement was specified, the model was meshed by

ANSYS. Figure 15 shows a zoomed in view of the refined mesh at the tunnel. Overall, including refinement, all cases of the CT scan model and the sawbone model contained around 60,000 elements, which was shown to be sufficient by resulting in only a 2% change in stress when more elements were used.

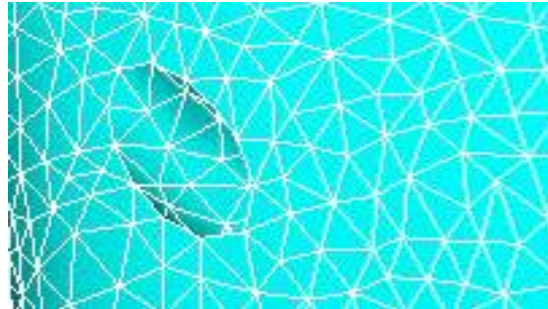


**Figure 15.** Refined mesh at AM tunnel exit

## **2.6 MATERIAL PROPERTIES**

### **2.6.1 Sawbone Model Material Properties**

The two models, CT scan and sawbone, required different material property assignments. The sawbone model, described in Section 2.2, was created as two parts, so uniform or homogeneous material properties were easily assigned to the cortical and cancellous regions of the femur. The cortical region was assigned a Young's Modulus of  $E=17,580$  MPA and Poisson's ratio of  $\nu=0.3$ . The cancellous region was assigned a Young's Modulus of  $E=280$  MPA and a Poisson's ratio of  $\nu=0.3$ . These properties were determined using values found in literature for these bone types (Reilly 1975, Rho 1993).

## 2.6.2 CT Scan Model Material Properties

In the CT scan model, material properties were assigned on an element specific basis. This was done using a method based on a process described in literature (Zannoni 1998), with modifications. The DIACOM files gathered from the CT scan and used to create the model in AMIRA, contain information that can be readily processed to derive physical relationships needed in the assignment of material properties to the finite element model. Each slice contains information regarding cortical bone, cancellous bone, tissue, and air (Figure 16). Each slice is also broken up into pixels (Figure 16), and each pixel contains a shade on the gray scale, which can later be related to density and then transferred as a Young's Modulus to each element in the finite element model. The DIACOM header files contain information on the size of each pixel and slice.

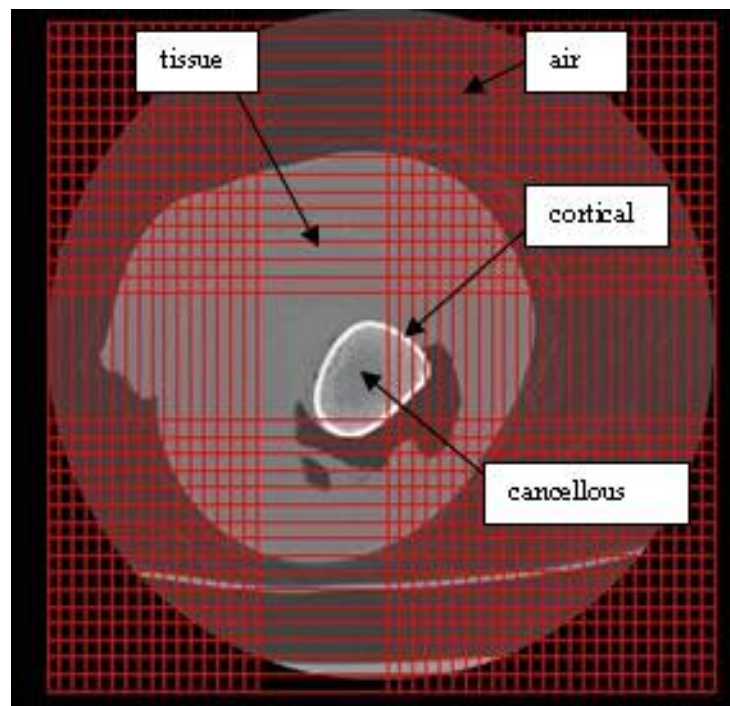


**Figure 16.** DIACOM image and approximate pixels

The technical computing program and language, Matlab (The MathWorks, Incorporated, version 2007a) was used to write a program to assign individual material properties to each element in the finite element model. Matlab's Image Processing Toolbox contains functions that can be used to process DIACOM files to output a radiographic density (RD) value corresponding to each pixel in the CT scan. A linear calibration between two points was required to obtain a density for each RD value output from MATLAB. Because the CT scan was performed in air, the RD value of air will be used as one calibration point. An average RD value in the cortical region and the apparent density value of cortical bone were used. Using these two values and performing operations on each element of the CT matrix, densities corresponding to each CT number or RD value can be calculated through the following equation (Zannoni 1998):

$$\rho(x, y, z) = \rho_1 + \frac{\rho_2 - \rho_1}{RD_2 - RD_1} [RD(x, y, x) - RD_1] \quad (3)$$

The density obtained from the CT scan data is then changed to a Young's Modulus value using the following relationship (Zannoni 1998):

$$E(x, y, z) = 4249\rho^3 \text{ (MPa)} \quad (4)$$

This empirical equation relates density and Young's Modulus for bone in the femur region. Utilizing these functions, a Matlab code was developed to extract the RD values for each pixel, convert these values to a corresponding density and then Young's Modulus, and relate the location of each pixel of the CT scan to each element in the finite element model. A Poisson's

ratio of  $\nu=0.3$  was used for all elements because both cortical and cancellous bone are approximated as having this value (Reilly 1975, Rho 1993).

Before this information could be related to the finite element model to assign heterogeneous material properties, the location of each element centroid contained in the model was needed to match the appropriate density. The three dimensional location of each centroid was gathered in ANSYS by using a macro, which is a file containing code that can be easily read by ANSYS. This information was then written to a data file, which could be read by Matlab. Using the centroid locations combined with the density information from the CT scan, a macro file containing the material properties for each element in the mesh was obtained. This file was then read into ANSYS and successfully assigned material properties to each element. (See Appendix A for Matlab code.)

## **2.7    LOADING AND BOUNDARY CONDITIONS**

After the model was meshed and heterogeneous material properties assigned, it was then ready to be loaded and solved using the finite element software ANSYS. The model was first constrained, in all degrees of freedom, mid-shaft and loaded in compression with 2000 N total condylar force, 1000 N applied to each condyle, to simulate the load the femur experiences during normal gait (Morrison 1970). The model was loaded at 0 degrees flexion and along the transepicondylar line, or the horizontal line in which both condyles touch at the most distal point (Figure 17). In order to load the model along this line, a new coordinate system was set up so that the positive z-direction was the direction of loading.

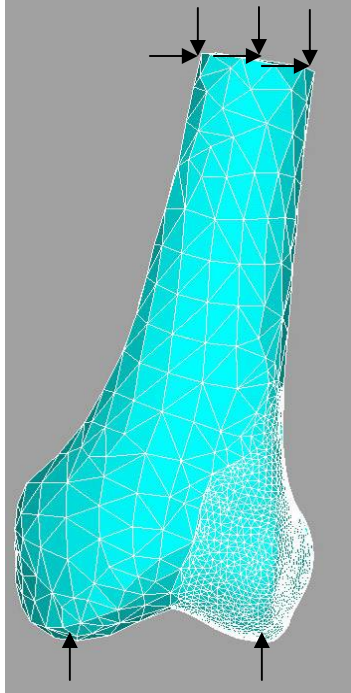


**Figure 17.** Meshed femur, loaded and constrained

Each case of the CT scan model and the sawbone model were solved in ANSYS using finite element analysis. After solving, element or nodal solutions could be obtained and plotted for stresses and strains. These values could then be compared between the cases of the CT scan model, the sawbone model, and experimental testing, which will be discussed in Chapter 4.

## **2.8 COMPUTATIONAL RESULTS**

### **2.8.1 Sawbone Model**

The sawbone model results include finite element analysis of the stresses for three different cases: intact, one tunnel, and two tunnels. Stresses were taken at positions located just proximal

to the tunnel exits, as these were found to be the area of highest stress, and taken to be the area of highest femur fracture risk. The model was loaded at 0, 30, 60, and 90 degrees of flexion, but only the results at 0 degrees of flexion are reported because it is at this position that the highest bone stresses were found. Thus, this position would have the highest risk of femur fracture. Figure 18 shows the contour plot of the one tunnel case. The highest stress concentration is seen in this figure to be at the tunnel exit.

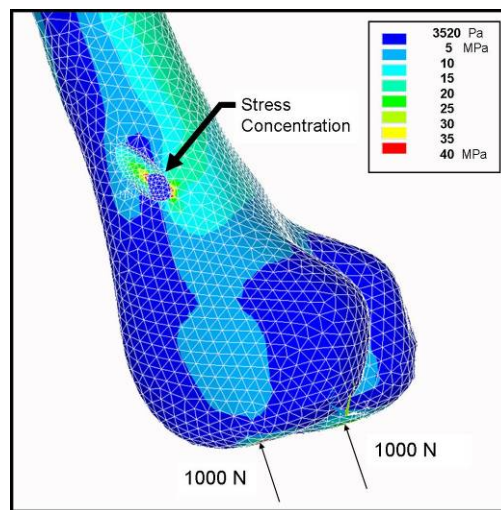


**Figure 18.** Location of highest stress concentration for one tunnel case

All cases were loaded, as discussed in Section 2.7. The resulting stress concentration factors were found along the tunnel axis for both the AM and PL tunnels at 0 degrees flexion. The stress concentration factor (SCF) at each point was determined by dividing the stress in the two tunnel or one tunnel case by the stress found in the intact case at the same location. Plots of SCF versus the distance along the tunnel axis are shown in Figures 19 and 20 for all three cases. In the plots, the tunnel entrance is at 0 mm, the AM tunnel exits the femoral shaft at 50 mm, and the PL tunnel exits at 30 mm.

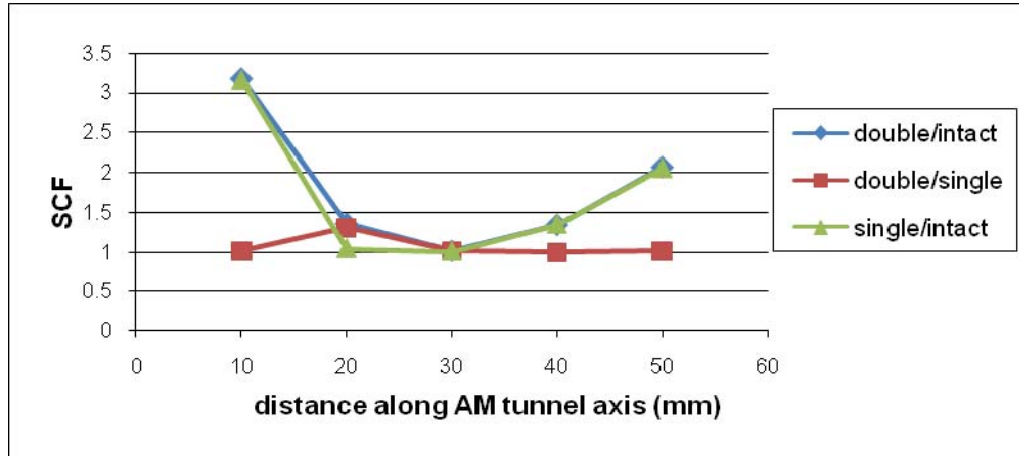


**Figure 19.** SCF for double, single, and intact cases vs. distance along AM tunnel axis for the sawbone model

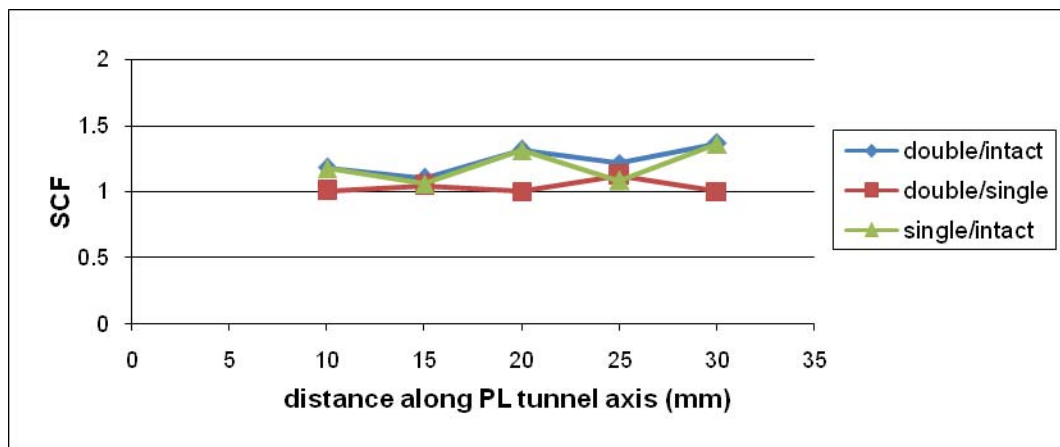


**Figure 20.** SCF for double, single, and intact cases vs. distance along PL tunnel axis for the sawbone model

The high stress concentration factor in both the double/intact and single/intact cases along the AM tunnel axis can be attributed to the close proximity of the AM tunnel entrance to the applied load. This causes an unnatural stress riser on the tunnel wall near the entrance, because of the point loads. Due to St. Venant's principle, as the stress is taken further away from the load, it no longer has such an effect. Assuming this unnatural stress riser is at the tunnel entrance, it can be said that the highest SCF is found at the tunnel exit. More specifically, according to the

sawbone model, the location just proximal to the AM tunnel exit contains the highest SCF as well as the highest stress (50 MPa).

### 2.8.2 CT Scan Model

The results for the CT scan model were first compared in a similar way as the sawbone model. Three cases—intact, single-bundle, and double-bundle—were meshed and solved in ANSYS after the assignment of material properties. The stresses were recorded along the distance of the AM and PL tunnel axes. A ratio of stress was calculated for the three cases just as it was in the sawbone model. Figures 21 and 22 show the resulting plots of stress concentration factor versus the distance along the tunnel axis.

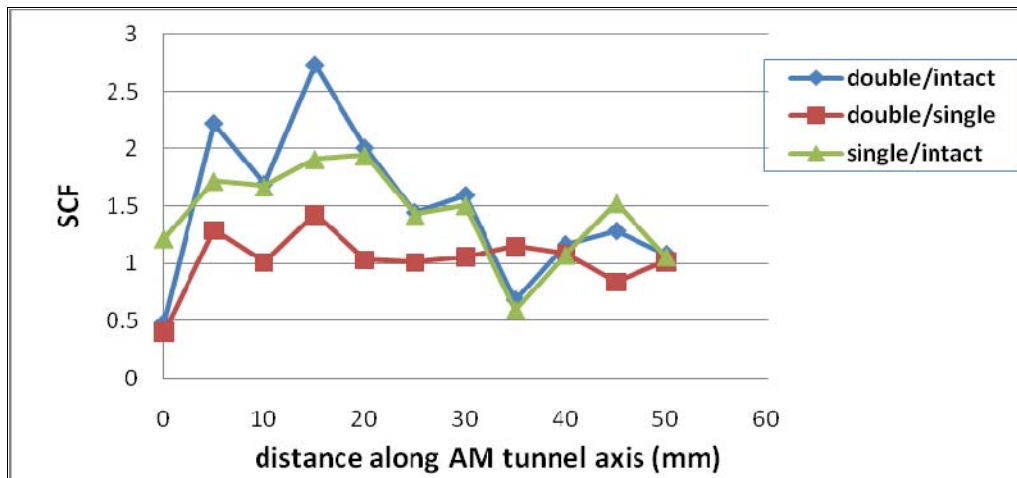


**Figure 21.** SCF for double, single, and intact cases vs. distance along AM tunnel axis for the CT scan model

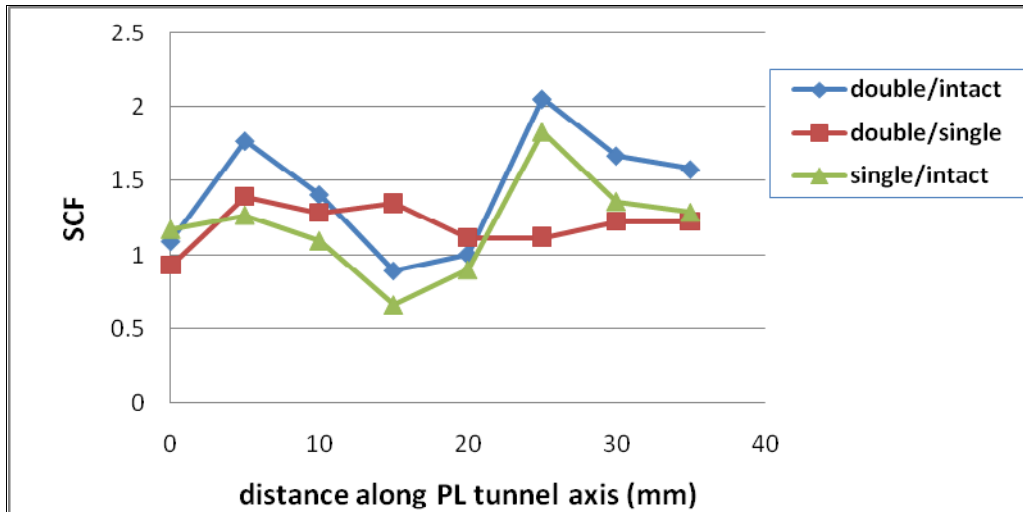


**Figure 22.** SCF for double, single, and intact cases vs. distance along PL tunnel axis for the CT scan model

As was the case with the sawbone model, there were high stresses recorded near the tunnel entrance and along the PL tunnel axis (around 200 Mpa). This can be attributed to the effect of the point load as the intact model also experienced high stresses. For both tunnels, the ratio of stress between the single- and double-bundle cases is between 1 and 1.5. This suggests that there are minimal increases in bones stresses with the addition of the PL tunnel.

### 2.8.3 Effect of Tunnel Position Variation

The results for the variations of the AM and PL tunnel locations, using the model created from the CT scan data, are shown in Figures 23 and 24. Each bar represents the maximum stress in either the AM or PL tunnel exit region (specified on graph), and found in the AM (Figure 23) or PL (Figure 24) tunnel variation case.

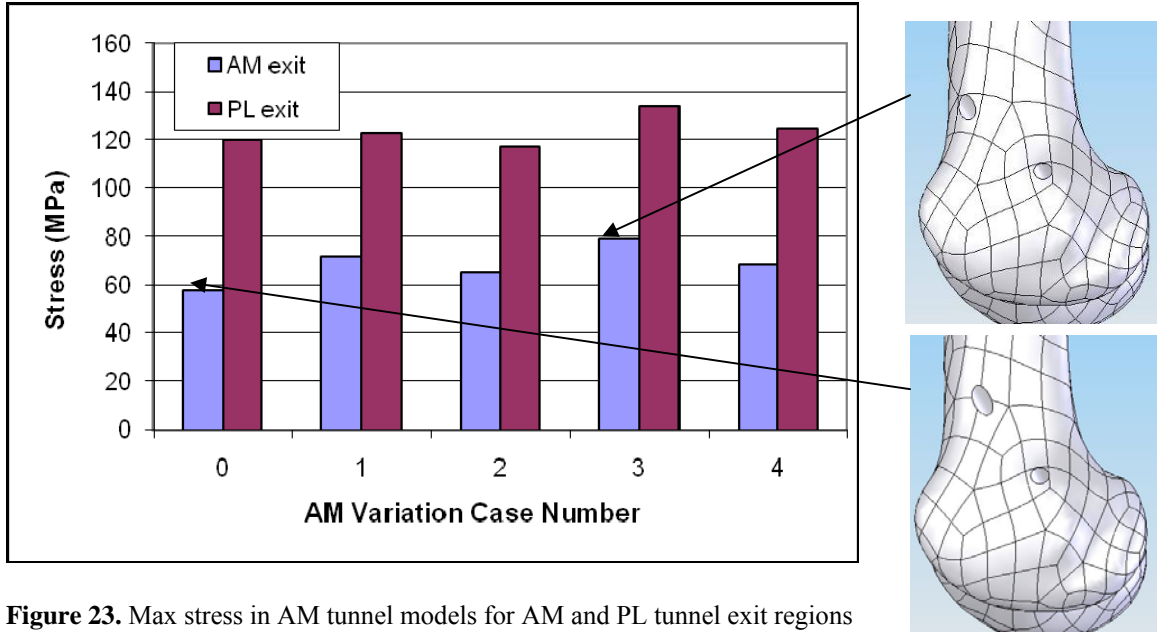


**Figure 23.** Max stress in AM tunnel models for AM and PL tunnel exit regions

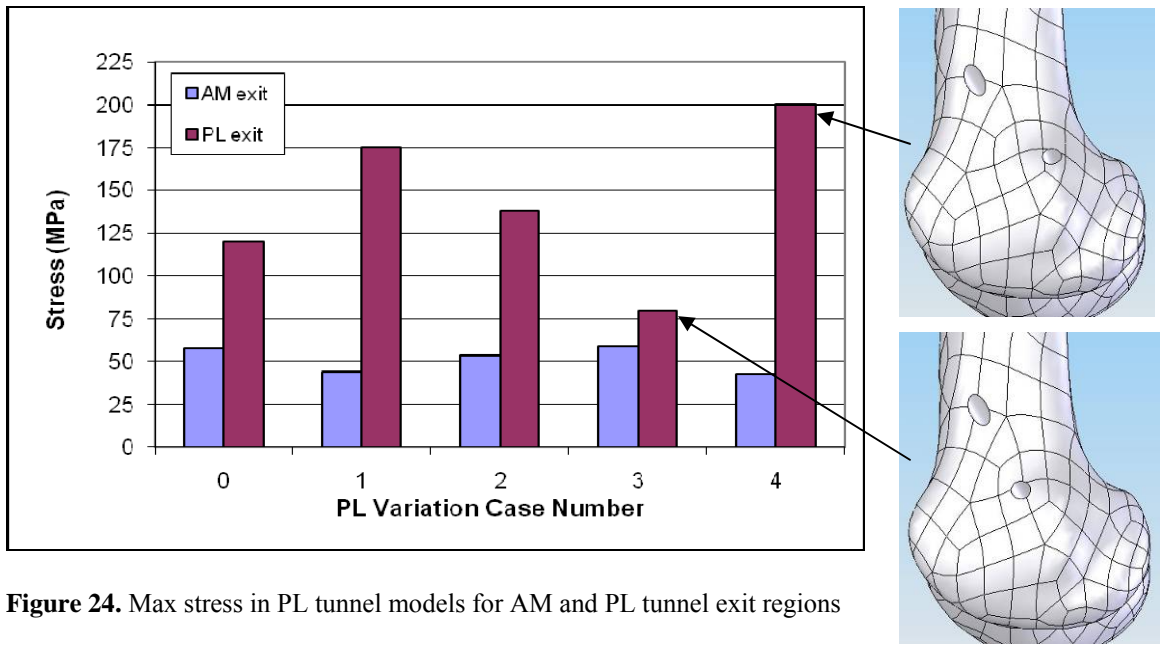


**Figure 24.** Max stress in PL tunnel models for AM and PL tunnel exit regions

When comparing the AM tunnel variation cases (Figure 23), it can be noted that when the AM tunnel axis is shifted 5 degrees anteriorly (AM 3) the bone stress at both tunnel exit regions

increases. When the AM tunnel axis is shifted 5 degrees medially (AM 2) the bone stress at the PL tunnel exit is only slightly lower than the standard case, while the standard case yields the lowest stress at the AM tunnel exit. When considering both the AM and PL stresses together, the standard case (# 0) appears to yield the best result, or the lowest stresses at both tunnel exit regions. Pictures depicting tunnel exits can be found next the graph in Figure 23. (Refer to Table 2 for tunnel positioning in the various models.)

For the PL tunnel variation cases (Figure 24), the lowest AM tunnel exit region stress is found when the PL axis is shifted 5 degrees posteriorly (PL 4). This orientation also produced the highest PL exit region stress. The lowest PL exit region stress was found when the PL axis was shifted 5 degrees anteriorly (PL 3); however, this orientation also yielded the highest AM tunnel exit region stress. Pictures depicting tunnel exits can be found next to the graph in Figure 24. When considering both AM and PL stresses together, the standard model (# 0) yields favorable results. (Refer to Table 2 for tunnel positioning in the various models.)

#### **2.8.4 Effect of Uniform and Stepped Diameter**

The results for the diameter variation models are shown in Figure 25. Each bar represents the maximum stress found in either the AM or PL tunnel exit region for the corresponding diameter case. Cases are specified on the graph as stepped-S or uniform-U, followed by the AM diameter/PL diameter. (Refer to Table 3 for specific stepped tunnel depths.)

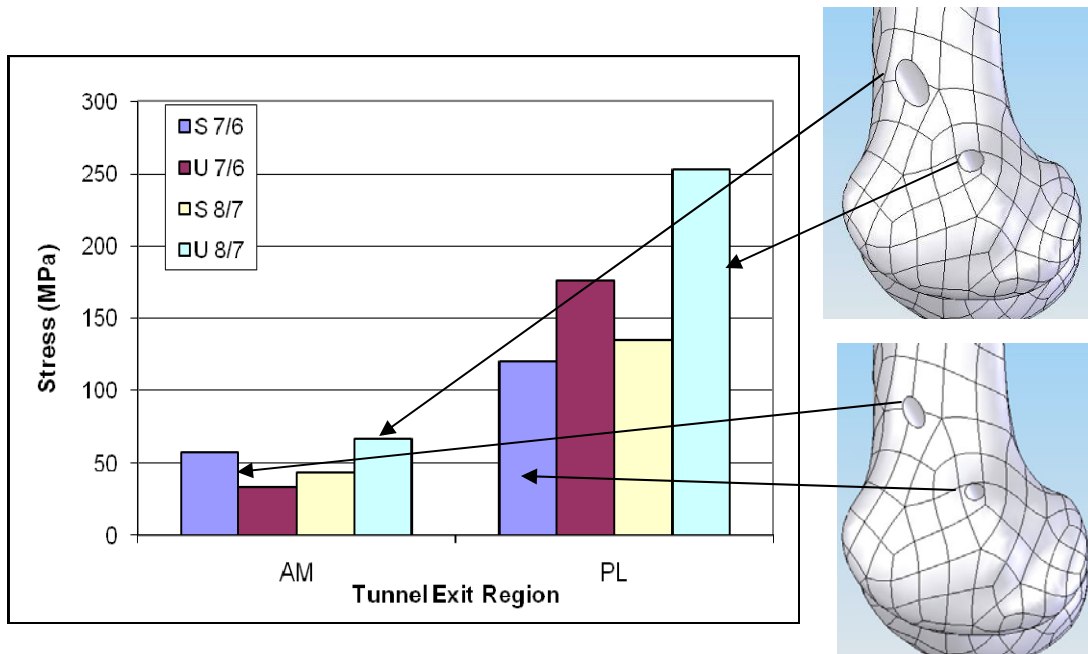


**Figure 25.** Max stress in AM and PL tunnel diameter models, stepped-S or uniform-U followed by AM/PL diameter

For the AM tunnel exit region, the U 7/6 case contains the lowest stress, but this case also contains one of the highest PL tunnel exit region stresses. The lowest PL tunnel exit region stress is found in the S 7/6 case. When considering both tunnel exit regions together, both the S 7/6 and S 8/7, the stepped tunnel cases, yield good results. Pictures depicting uniform and stepped tunnel diameter exit locations on the femoral shaft are shown next to the chart in Figure 25.

## 2.9 DISCUSSION OF COMPUTATIONAL RESULTS

From elastic theory, it is known that if opposing forces are applied to the top and bottom edges of a two dimensional plate and perpendicular to the axis of a hole through the center of the plate, the highest stresses will be found near the left and right edges of the hole and not the top and

bottom (Pilkey 1997). For both the sawbone and CT scan models, the highest stress was found just proximal (near the top) of the tunnel exits. However, this is not in contradiction with the previously stated theory because in the case of the three dimensional femur model, the tunnels are made at an angle and the loads are not applied perpendicular to the axis of the tunnel or parallel to the long axis of the femur. Thus, the area of highest stress in the model was not able to be predetermined by theories.

### **2.9.1 Sawbone vs. CT Scan Model**

Upon examination of the AM and PL tunnel variation cases as well as the diameter variation cases for the CT scan model, one can see that the PL tunnel exit stress is higher than that at the AM tunnel exit. The results of the sawbone model, found the opposite to be true. According to the sawbone model, the highest stress in all cases was found at the AM tunnel exit. The difference between the two findings can be attributed to the differences in the two models. The CT scan model was developed from a scan of a human knee and has heterogeneous material properties, whereas the sawbone model is a replica of the geometry of the femur and has two distinct parts with each part having homogenous material properties. The geometry of the two models also differed. The sawbone model had smoother and rounder condyles while the CT scan model had a more rigid and uneven shape (Figure 26). Thus, due to the material properties and femur geometry, the stress distribution differed between the two models of the femur.

Another explanation for the high stress at the PL tunnel exit region in the CT scan model is the loading used. The PL tunnel was closer to the point load than the AM tunnel and may have been affected by the point load, which would cause an unrealistically high stress at this tunnel. The intact CT scan model also had much higher stresses than expected for cortical bone in the

PL tunnel region (150 MPa), even though no tunnel was present. This loading has more effect on the CT scan model than the sawbone model, because the overall tunnel exit locations are lower in the CT scan model and the geometry between the two is different, thus affecting how the stress is distributed throughout the condyles (Figure 26).



**Figure 26.** Lateral view of models depicting difference in tunnel placement and exit diameter used in CT scan (left) and sawbone (right) models

The ultimate and yield stresses of cortical bone are 195 MPa and 182 MPa respectively in the longitudinal direction (Cowin 1989), which is much greater than all but two of the stresses found when using the normal gait load of 2000 N in the model. In the two CT scan model cases that resulted in higher stresses (PL 4, U 8/7), the location of high stress was in the PL exit region when the tunnel exit was more distal or larger. Thus, this value of stress is most likely large due to the closeness of the tunnel exit to the point load applied. Higher loads would be needed to reach the ultimate stress in other areas of the bone.

In future studies, loading conditions that are better able to represent physiological loading in the knee should be used. This can be done with a loading function, which will assign loads to each node or element on the condyle, or a pressure distribution. Also, a tibia model could be

developed and used in combination with the femur model to apply physiological contact forces on the condyles.

### **2.9.2 Tunnel Location and Diameter**

The results of this study can be used to derive an estimate of the tunnel location and diameter that cause the least amount of bone stress; however, these results should be verified with new modeling and experimental testing. The tunnel location results show that the standard case (see Table 2 for tunnel locations) produces the lowest stresses when considering both tunnel exit regions. As the AM tunnel exit becomes higher up the femoral shaft (AM 2) or more anterior (AM 3), the stress in the AM tunnel exit region becomes higher (Figure 23). The stress also rises when the PL tunnel exit is more posterior (PL 1 and PL 4, see Figure 24). When the AM and PL tunnel exits become closer together (AM 1, PL 2, and PL 3), the stress in both regions varies as to whether it is higher or lower than that of the standard model (Figures 23 and 24).

The tunnel diameter cases that produced the lowest stresses for both the AM and PL tunnel exit regions were those containing a smaller exit diameter (S 7/6 and S 8/7, see Figure 25). This finding would suggest that the Endo-Button fixation device would contribute least to increased stresses in the femur, as a result of the smaller exit diameter of the tunnels. Thus, according to this data, other femoral fixation devices would create a higher risk for femur fracture.

### **3.0 EXPERIMENTAL TESTING**

#### **3.1 TEST SPECIMENS**

The goal of the experimental testing was to validate the computational models of the femur. To accomplish this, actual human cadaver femurs were tested in axial compression. Human cadaver parts are expensive to purchase, so femurs that were already used for a previous study were reused for this study. The initial study involved analyzing the pressure between the femur and the tibia as it relates to the ACL. Low loads were used and the femurs were not damaged. Thus, it was suitable to reuse these femurs for the current study.

These femurs had been previously used, and proper IRB (institutional review board) protocol was followed, and approval was granted. Eleven fresh frozen femurs were allowed to thaw and then dissected by a qualified surgeon to remove all soft tissue. The bone was then ready for strain gage attachment, and testing.

## 3.2 TEST EQUIPMENT

### 3.2.1 Compression Testing Machine

The equipment used in the testing include: ATM (axial testing machine), load cell, fixation device, strain gage rosettes, strain gage kit, and strain gage reader (Figure 27). The ATM allows for compression and tension testing of various objects, or specimens, in a variety of orientations. For the purpose of this study, the ATM will be used for uniaxial compression testing.

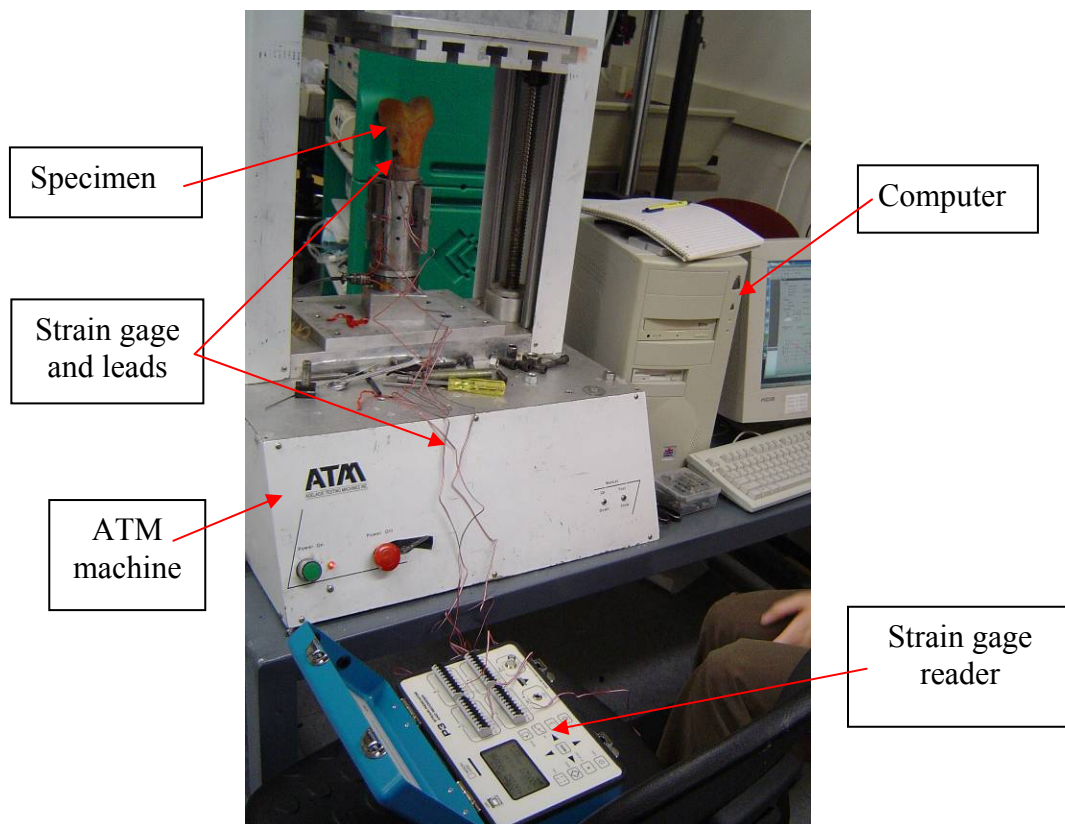


**Figure 27.** Test equipment set-up

The machine is electrically connected to a computer containing software that controls the machine. The load cell is attached mechanically to the ATM (underneath the femur) and

electrically to the computer. The proximal end of the specimen is potted with a fast drying cement in the shape of a cylinder, so that it can be easily inserted into the fixation device attached to the base of the machine. The metal plate on the top of the machine moves vertically to apply a compressive load to the condyles of the femur. As contact is made between the plate and the femur, the computer shows the reading of the load cell in Newtons.

### **3.2.2 Strain Gage Attachment**

Stacked rectangular strain gage rosettes were chosen for this application because the direction of principle strain was not known. The gages were ordered from Vishay Micro-Measurements (C2A-06-125WW-350), and had a gage factor of 2 and resistance of 350 ohms. This particular gage is encapsulated and ready for attachment on a variety of surfaces, including moist surfaces. They were attached to the femoral shaft, near the AM tunnel exit. This location was chosen, because it was shown in the computational models to be an area of high stress (see Section 2.8). Before a gage was attached to the cadaver femur, the skill of gage attachment was practiced on sawbone femurs and small pieces of goat femur bones.

The process of mounting a gage on a surface requires a precise procedure. First, the surface was sanded with three different grades of sand paper, beginning with a coarse grade and moving to a fine grade. During sanding, the surface was cleaned with a neutralizer. Then, the gage was prepared by placing it front side down onto a clear piece of tape. Once the surface was dry, a general purpose strain gage adhesive (M-Bond 200) was used to coat the back side of the gage. Next, a small drop of super glue was placed on the surface and the gage was immediately pressed on top and held tightly with a finger for a few minutes. Finally, the tape was peeled from the top of the gage, leaving the gage itself securely mounted to the surface. After the gage was

attached, the leads from the gage were connected to a strain gage reader. The reader was used to record the strain readings for various loads.



**Figure 28.** Composite sawbones

Before testing was performed on actual human femurs, sawbones were used as practice. The sawbones were made of a composite material meant to closely replicate bone. They had a small canal through the center of the bone, along the femoral shaft, as shown in Figure 28. Thus, these sawbones could not be used for actual comparison, as the canal would alter the tunnel placement and strain, but they were used for practice. A UPMC surgeon drilled tunnels in the sawbones to imitate those drilled in surgery. These bones were then potted with the fast drying cement and a strain gage was attached just proximal of the AM tunnel exit using the method previously described (Figure 29). The sawbones were then tested in compression using the ATM machine.

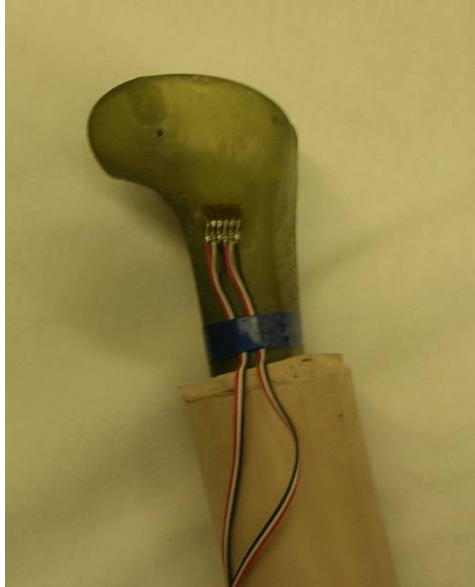


**Figure 29.** Strain gage attached to potted sawbone

The same process of gage attachment was also used to mount the gages onto the human femur cadavers (Figure 30). Extreme care had to be used during the attachment process due to the wet and porous nature of the bone, which was much different the dry and impermeable surface of the sawbone. The area outside of the AM tunnel, on the femoral shaft, was sanded to make sure it was as flat and smooth as possible. This area was then allowed to dry briefly to ensure a good surface for attachment. The adhesive and glue were then used to secure the gage to the bone.

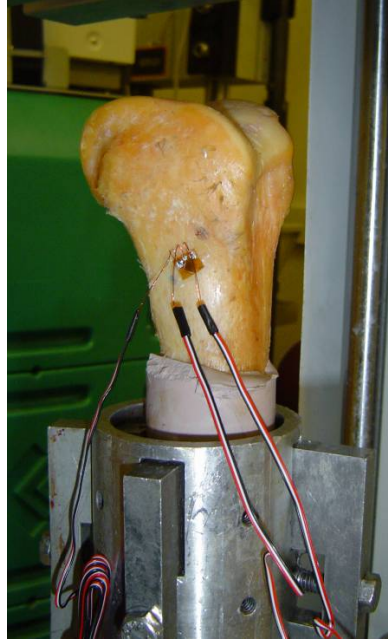


**Figure 30.** Cadaver with mounted gage, set up for testing

### 3.3 TESTING PROTOCOL

After the gage was properly attached and the bone was inserted into the ATM machine (Figure 27), the compression testing could begin. Loads were applied from 100-1300 N in 100 N increments at a rate of 10 N/s, and the strain was recorded from the strain gage reader at each load for all three gages. Then, a formula for principal strain from the three individual gage readings from the strain gage rosette was derived from the following formulas for principle strain and shear strain, as related to a rectangular rosette (Riley 2002).

$$\varepsilon_{p1,p2} = \frac{\varepsilon_x + \varepsilon_y}{2} \pm \sqrt{\left(\frac{\varepsilon_x - \varepsilon_y}{2}\right)^2 + \left(\frac{\gamma_{xy}}{2}\right)^2} \quad (5)$$

$$\varepsilon_2 = \varepsilon_x \cos^2 45 + \varepsilon_y \sin^2 45 + \gamma_{xy} \sin 45 \cos 45 \quad (6)$$

By aligning the coordinate system such that the x-axis is the same as the first measured strain, the y-axis is the same as the third measured strain, and using the above formula for the second measured strain, Equation 5 becomes Equation 7 below. This equation will be used to determine the maximum principle strain in all of the experimental testing.

$$\varepsilon_{p1,p2} = \frac{\varepsilon_1 + \varepsilon_2}{2} \pm \frac{1}{\sqrt{2}} * \sqrt{(\varepsilon_1 - \varepsilon_2)^2 + (\varepsilon_2 - \varepsilon_3)^2} \quad (7)$$

### 3.4 EXPERIMENTAL TESTING RESULTS

The maximum principle strain calculated, from Equation 7, at each load was used to report the experimental results. These results were then plotted as micro-strain versus compressive load applied, in Newtons. The maximum principle strain results of both the sawbone and CT scan computational finite element models at the same loads were also plotted. These values were obtained by finding the maximum principal strain in the element on the model nearest to the location of the actual gage application on the cadaver specimen. By reporting the results from both experimental and computational data in the same way, a direct comparison can be made between the two. Thus, the computational results for strain are also reported in this section.

### 3.4.1 Statistical Analysis

A least squared analysis was used to determine the linearity of the experimental lines plotted as micro-strain versus load. Table 4 shows the resulting r-squared value used to measure linearity (1 being linear), and the slope of each line. Table 5 gives the average and standard deviations of the cadaver results for better comparison.

**Table 4.** R-squared value and slope for cadavers and computational models when plotted as micro-strain vs. load

| <b>Femur/Model</b> | <b>r<sup>2</sup></b> | <b>Slope</b> |
|--------------------|----------------------|--------------|
| CT scan            | 1                    | 0.318        |
| sawbone            | 1                    | 0.299        |
| cadaver 1          | 0.9909               | 0.1529       |
| cadaver 2          | 0.9634               | 0.2119       |
| cadaver 3          | 0.9861               | 0.1532       |
| cadaver 4          | 0.993                | 0.2707       |
| cadaver 5          | 0.9971               | 0.3531       |
| cadaver 6          | 0.9989               | 0.1415       |
| cadaver 7          | 0.9986               | 0.1825       |
| cadaver 8          | 0.9986               | 0.1579       |
| cadaver 9          | 0.9875               | 0.3591       |
| cadaver 10         | 0.992                | 0.3463       |
| cadaver 11         | 0.9997               | 0.3026       |

**Table 5.** Average and standard deviation for r-squared value and slope of cadaver results

|                | <b>average</b> | <b>std dev</b> |
|----------------|----------------|----------------|
| r <sup>2</sup> | 0.9914         | 0.0104         |
| slope          | 0.2392         | 0.088764       |

Using the student's t-test (Devore 2004) for comparison of a mean to a hypothesized value, there was shown to be no significant difference between the slope values of the cadaver tests and the models. The mean used in this test was taken from the slope of the cadaver results and the hypothesized value is the computational slope value from the models. The two models differed in slope by less than 0.02, thus an average of 0.3 was used as the hypothesized slope in the test. The relationship between strain and load was shown to be close to linear (i.e.  $r^2=1$ ), for cadavers 1-11 using this same t-test. In this case, the mean r-squared value of the cadaver results was compared to the hypothesized value of one and no significant difference was found.

The value of strain was also analyzed at each load for both models and cadavers. Figure 31 shows the resulting strains at 1000 N in compression. Using the same statistical analysis, there was shown to be no significant difference among the values of strain at each load. The two computational models differed by less than 20 micro-strain at each load, and the values were averaged for use in the analysis. This computational strain was then compared to the mean strain of all cadavers tested and no significant difference was found. All statistics are reported at the 98% confidence level. (See Appendix B for further detail of the statistical analysis including graphs of strain at each load.)

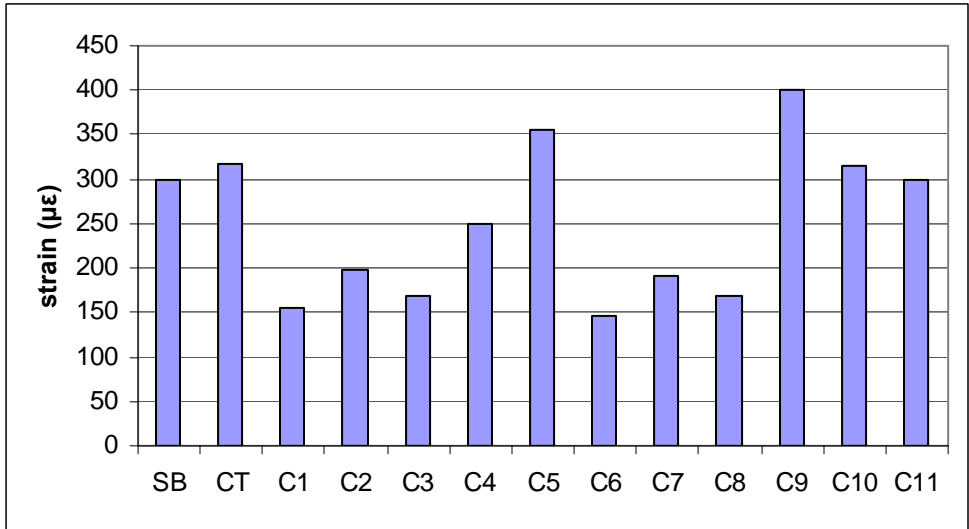


**Figure 31.** Chart showing strain ( $\mu\epsilon$ ) at 1000 N for sawbone model (SB), CT scan model (CT) and cadavers 1-11 (C1-C11)

## **4.0 DISCUSSION**

### **4.1 COMPUTATIONAL VS. EXPERIMENTAL**

The results of the experimental cadaver tests will be compared to the results of the sawbone and CT scan computational models in this section. The results of the computational models suggest three things. First, that there is no increased risk of femur fracture following the DB ACL reconstruction when compared to the SB ACL reconstruction. Second, slight variations in tunnel placement do not significantly affect stresses in the femur bone. Third, a larger, constant tunnel diameter increases bone stress in the femur near the tunnel exit area. The purpose of conducting the experimental study was to validate the computational models and these results obtained from the stress analysis.

The experimental study results support the validity of the computational results obtained from the sawbone and CT scan models. As shown in Section 3.4, there was no significant difference between computational and experimental results for strain. Though there were some slight differences between slope and linearity, they were not found to be significant. These slight differences can be attributed to the heterogeneous material properties of bone, which differ from specimen to specimen when using cadavers, and remain constant in the CT scan model. Also, the homogenous material properties of the sawbone model may have caused difference between the two computational results as well as the experimental results. The steeper slope of both the sawbone and CT scan models suggests a stiffer material than that of the cadavers. This may be due to the loading techniques used in the experimental and computational testing. Although both

cadaver specimens and models were loaded with 2000 N, the loading methods were different. In the computational testing, a single point load was applied to each condyle; however, in the experimental testing, a flat plate was lowered and pressed against the condyles causing a distributed load.

In the future, more physiological loading should be modeled by using the tibia-femoral joint. Eventually, an entire knee joint could be modeled to most accurately mimic physiological movement and loading. A cadaver knee could then be tested at various loads and the results compared to the knee model. Strain gages should be applied at different locations around the tunnel exits, near the condyles, and along the femoral shaft for determination of the location of the highest experimental strain as it may differ from that found in the model. Also, specimen specific CT scan models could be created and validated by experimental testing, which would allow for direct comparison as both model and cadaver would have the same material properties and geometry.

## APPENDIX A

### MATLAB CODE TO ASSIGN MATERIAL PROPERTIES

The following Matlab code was used to assign element specific material properties to each element in the meshed finite element model. The code required the x, y, and z locations of the element centroids of the model. These were obtained using the following code in ANSYS, and modifying it three different times.

```
*DIM, NODESZ, ARRAY, (# of elements in model), 1, 1, elem(x, y, or z), XYZ,, 0
*DO,i, (# of elements in model),1
*GET,Z,ELEM,i,CENT,(X, Y, or Z)
NODESZ(i,1,1)= (X, Y, or Z)
*ENDDO
/OUTPUT, nodes(X, Y, or Z), txt,
*vwrite,NODES(X, Y, or Z)(1,1,1)
(E10.4,2X)
```

The previous code steps through each element, as numbered in ANSYS, and stores the x, y, or z coordinates in an output file called NODES(X, Y, or Z). The output file is then saved as an m-file, for use in Matlab, with the following heading (for the x centroid location):

```
function [xc]=centX()  
xc=[
```

The bracket should be closed at the end of the list of centroids, and the same header used for the y and z centroid locations, substituting y and z for x respectively.

After all three files containing element centroid information are stored in this manner, the code which calculates the material properties from the CT scan data can then be run. This code uses information contained in the DIACOM files about each pixel and slice thickness. The following information is obtained from the files:

Slice Thickness = 1 mm

Spacing between slices = 1 mm

Rows = 512

Columns = 512

Reconstruction diameter = 200 mm

Data collection diameter = 480 mm

Each slice, or 2-D image of a cross-section of the femur, is a square whose dimensions are calculated in the Matlab code. The software program Amira, which is used to create the

model from the CT scan, gives the local axis coordinates of a corner of this square based on the global axis. This corner becomes the starting point for relating voxels to elements in the Matlab code. The global origins of the CT scan and FE model are the same; therefore, the same coordinates for the starting point (i.e. the corner of the square) can be used in ANSYS as well.

Finally, the code saves the calculated material properties with their corresponding elements to a macro file that can be read by ANSYS to assign material properties. Below is the Matlab code:

```

%%M. E. O'Farrell (revised summer 2007)
%%Summer 2006 DB ACL femur fracture study
%%Code will read in CT data and calculate element specific
%%elastic modulus based on element centroid location.
%%Required files are: centX, centY, centZ.m (centroids)
%%All diacom files from CT scan

clear
clear all

nSlices = 152;      %Number of slices or *.dcm files minus one
nFrames=(nSlices-1); %number of frames for entire CT data is 151 slices

display('loading slices')
for i = 640:(nFrames+640)
    fname =
sprintf('I.1.2.840.113619.2.30.1.1762813188.1779.1133357394.%d.dcm', i);
    slicenum=i-639;
    CT(:, :, slicenum) = dicomread(fname);
end

display('finished loading slices')

%%See Medical Engineering & Physics 20 (1998) 735-740%%
% %%%%%%%%%%%%%%%%%%%%%%%%%%%%%%%%%%%%%%%%%%%%%%%%%%%%%%%%%%%
%%Assign RD # and density to average cortical region%%
RD1 = 1840;    %units: HU

roel = 1.73;  %units: g/cm^3

%%%%%%%%%%%%%%%%%%%%%%%%%%%%%%%%%%%%%%%%%%%%%%%%%%%%%%%%%%

%%CT scan was done in air (min(CT) = -1024)

CTmin=min(min(min(CT)));

```

```

RD2 = double(CTmin);
roe2 = 0;

%%%%%%%%%%%%%%%%%%%%%%%%%%%%%%%%%%%%%%%%%%%%%%%%%%%%%%%%%%%%%%%%%%%%%%%%

%%Linear interpolation to find densities of each pixel%%%%%%%%%%%%%%%%%%%%%%%%%%%%%%%%%%%%%%%%%%%%%%%%%%%%%%%%%%%%%%%%
%%Calculate densities and E in one expression to reduce runtime%%%%%%%%
%%E=k*roe^3, k=4249, units of k: GPa(g/cm^3)^(-3);
display('calculating densities and Elastic modulus in one expression.....')

E = (((roe1 + ((roe2 - roe1) / (RD2 -
RD1))*(double(CT(1:512,1:512,1:nSlices)) - RD1)).^3)*4249);

%Set up origin%%%%%%%%%%%%%%%%%%%%%%%%%%%%%%%%%%%%%%%%%%%%%%%%%%%%%%%%%%%%%%%%%%%%%%%%
i=730; %index number on diacom files

finfoname=sprintf('I.1.2.840.113619.2.30.1.1762813188.1779.1133357394.%d.dcm'
, i);
    info=dicominfo(finfoname);

nRows = info.Rows;
nCols = info.Columns;
ReconDiam = info.ReconstructionDiameter;
DCollDiam = info.DataCollectionDiameter;
SpacingBetweenSlices=info.SpacingBetweenSlices;

%calculate voxel dimensions

xv = ReconDiam/double(nRows)/10; %in cm
yv = ReconDiam/double(nCols)/10;
zv = SpacingBetweenSlices/10;

%Fix starting point for CT space according to local coordinate system in CT
%scan and z coordinate of first slice used.
%check AMIRA for this if trying different CT scans

fixX=(-8.98); %in cm
fixY=(-9.13);
fixZ=(-1.25);

%%Set up vectors defining Voxel coordinates

X = [ fixX : xv : ((511*xv)+fixX)]; %in cm
Y = [ fixY : yv : ((511*yv)+fixY)];
Z = [ fixZ : zv : ((zv*nFrames)+fixZ)]; %must load all frames!!!!

display('loading centroids.....')

%%Load 3 vectors of element centroids

xc = [centX]; %in cm
yc = [centY];
zc = [centZ];

```

```

numcentroids = length(xc); %scalar number of elements

%%Find voxel closest to element centroid
%%Assign voxel closest to element centroid, that element's E value

display('Compare FEM centroids to CT coordinates and assign E values')

x=1;
for i = 1:1:numcentroids %step through in order of centroids

    IX1 = find(X > xc(i));
    IX2 = find(X < xc(i));

    if (abs(xc(i) - X(IX1(1)))) < abs(xc(i) - X(IX2(length(IX2))))
        CTxindex = IX1(1);
    else
        CTxindex = IX2(length(IX2));
    end

    IY1 = find(Y > yc(i));
    IY2 = find(Y < yc(i));

    if (abs(yc(i) - Y(IY1(1)))) < abs(yc(i) - Y(IY2(length(IY2))))
        CTyindex = IY1(1);
    else
        CTyindex = IY2(length(IY2));
    end

    IZ1 = find(Z > zc(i));
    IZ2 = find(Z < zc(i));

    %%correction for when IZ2=0%%

    if IZ2~=0
        LIZ2=IZ2(length(IZ2));
        ZLIZ2=Z(IZ2(length(IZ2)));
    else
        LIZ2=0;
        ZLIZ2=0;
    end

    if (abs(zc(i) - Z(IZ1(1)))) < abs(zc(i) - ZLIZ2)
        CTzindex = IZ1(1);
    else
        CTzindex = LIZ2;
    End

    %Track element numbers that correspond to CT#s

    CTtoELEMx(i) = CTxindex;
    CTtoELEMy(i) = CTyindex;
    CTtoELEMz(i) = CTzindex;

    %E will be in units of GPa!!

```

```

ECENT(i) = E(CTxindex,CTyindex,CTzindex);

%Produces vector of elastic modulus in order of element centroids input above

% Fix zero errors in ECENT vector
% Find pixels that are not composed of air
% Otherwise, E will equal zero, which creates errors in ANSYS

e = 1;
while (ECENT(i) < 1)
    if (E(CTxindex + (1*e),CTyindex,CTzindex) > 0)
        CTxindex = CTxindex + (1*e);
        ECENT(i) = E(CTxindex,CTyindex,CTzindex);
    elseif (E(CTxindex,CTyindex + (1*e),CTzindex) > 0)
        CTyindex = CTyindex + (1*e);
        ECENT(i) = E(CTxindex,CTyindex,CTzindex);
    else
        display('out of bounds')
    end
    e = e + 1;
    VOXELERROR(i) = e;

end

end

%end of big for loop

%%%%%Create ANSYS Macro to assign material properties to element numbers

%Assign E, PRXY, values to material reference numbers

fid = fopen('materialprop.mac', 'w');
fprintf(fid,'!M. OFarrell, modified Summer 2007\n');
fprintf(fid,'!This Macro assigns the calculated E values to\n!their
respective elements with a constant\n!poissons ratio as 0.3\n');
fprintf(fid,'/PREP7\n')    %Enter prep7 processor
for i = 1:length(ECENT)
    stringnameEX = sprintf('MP,EX,%d,%d\n',i,ECENT(i));
    stringnamePRXY = sprintf('MP,PRXY,%d,0.3\n',i);
    fprintf(fid,stringnameEX);
    fprintf(fid,stringnamePRXY);
end

%Assign element numbers to material reference numbers

for i = 1:1:length(ECENT)
    stringname = sprintf('MPCHG,%d,%d\n',i,i);
    fprintf(fid,stringname);
end

fclose(fid)

%end of code

```

## **APPENDIX B**

### **STATISTICAL ANALYSIS FOR EXPERIMENTAL TESTING**

The statistical analysis used to determine the linearity of the experimental testing results and to compare the experimental and computational results will be discussed here. The student's t-test for small sample sizes was used to compare the mean of the cadaver results to a hypothesized value, or the computational value. The slopes of the cadaver results when plotted as strain versus load applied, the linearity of these lines, as well as strain values at a given load were analyzed using this test.

The following graphs show the micro-strain of the sawbone model (SB), CT scan model (CT), and cadavers 1-11 (C1-C11) at each load tested (100 N to 1300 N by 100 N increments). These graphs were used to determine the distribution of strain at each load, and whether or not there was a significant difference between the mean value of strain for the cadavers tested and the computational value from the models. As stated in Chapter 3, no significant differences were found at 98% confidence level. However, it should be noted that there is a wide variation in values of strain from the experimental testing. Future testing should be done to verify the results from the experimental and computational comparison.

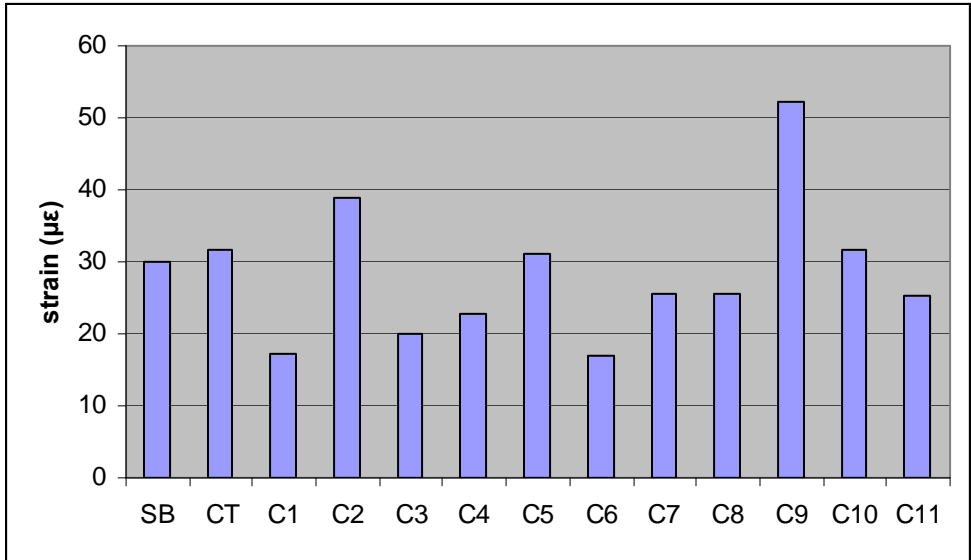


**Figure 32.** Chart showing strain ( $\mu\epsilon$ ) at 100 N for all models and cadavers

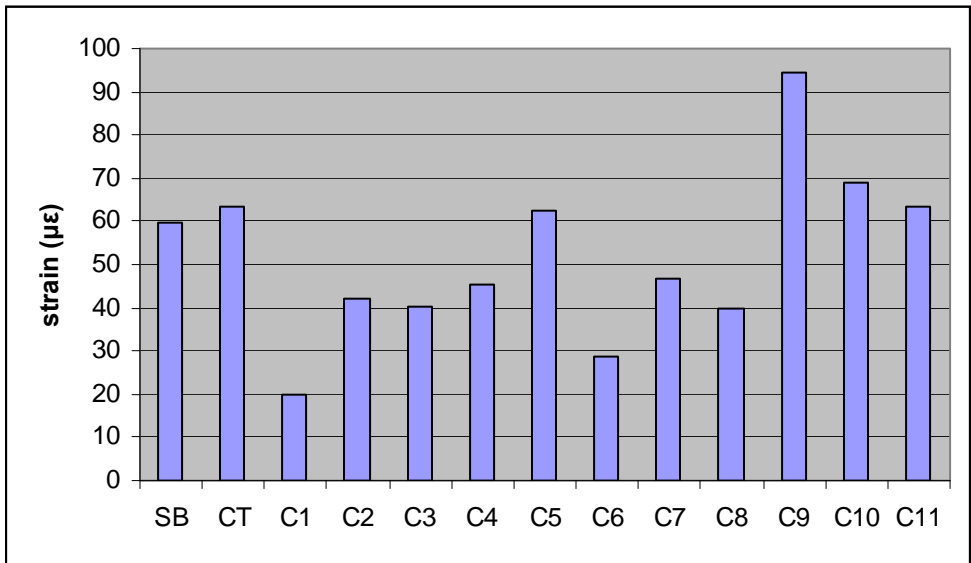


**Figure 33.** Chart showing strain ( $\mu\epsilon$ ) at 200 N for all models and cadavers

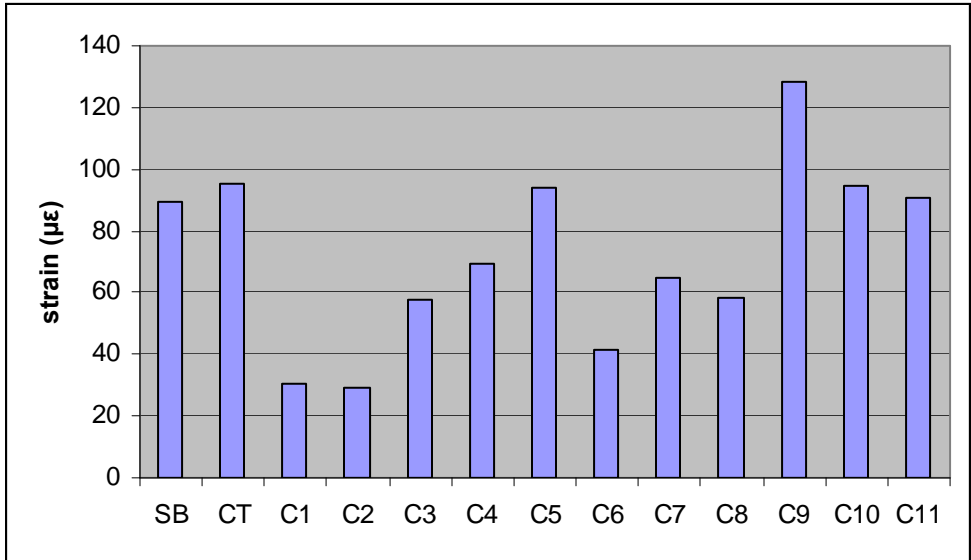


**Figure 34.** Chart showing strain ( $\mu\epsilon$ ) at 300 N for all models and cadavers

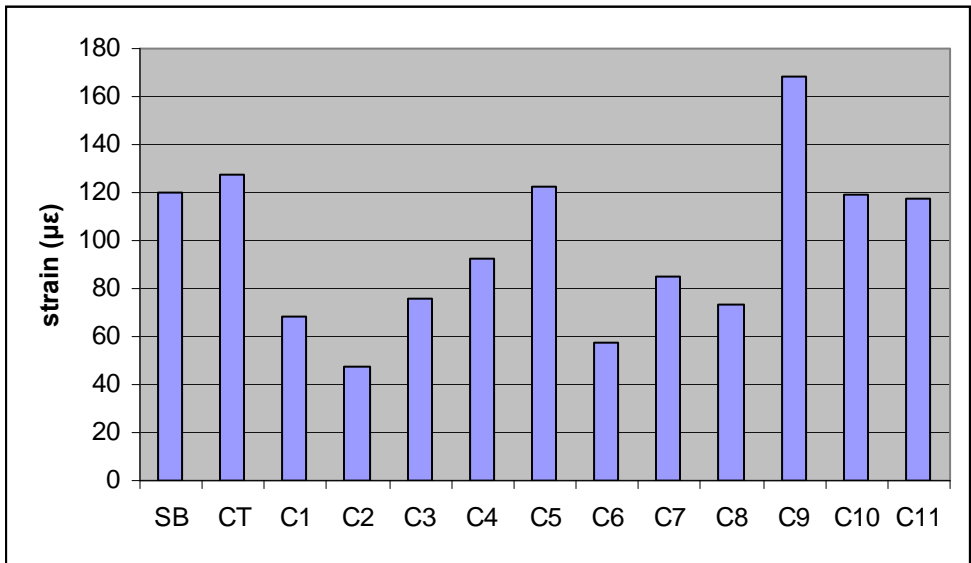


**Figure 35.** Chart showing strain ( $\mu\epsilon$ ) at 400 N for all models and cadavers

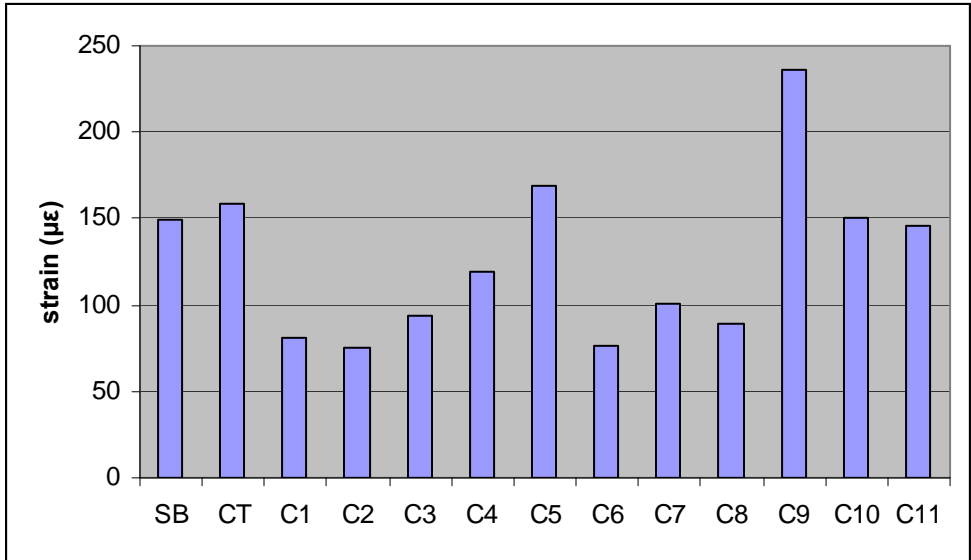


**Figure 36.** Chart showing strain ( $\mu\epsilon$ ) at 500 N for all models and cadavers

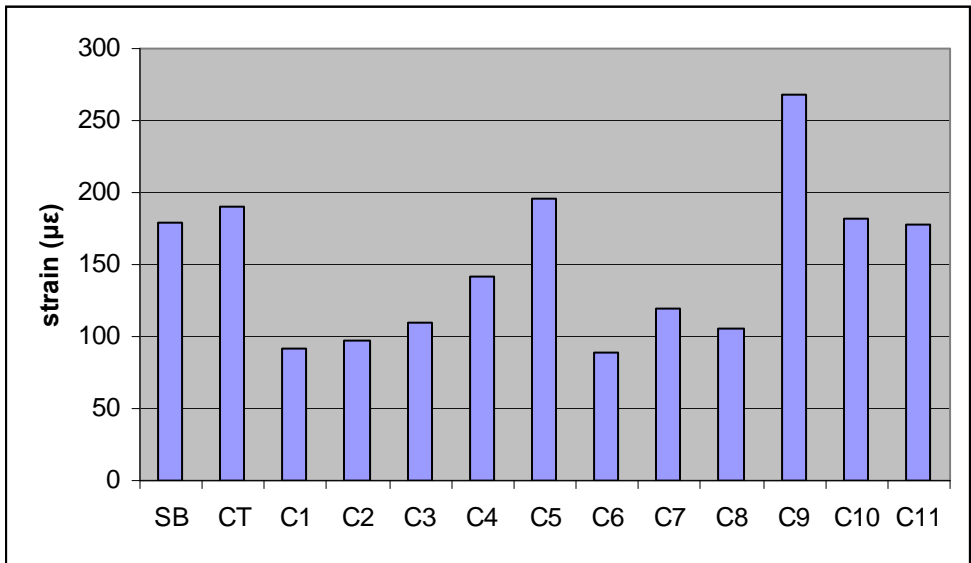


**Figure 37.** Chart showing strain ( $\mu\epsilon$ ) at 600 N for all models and cadavers

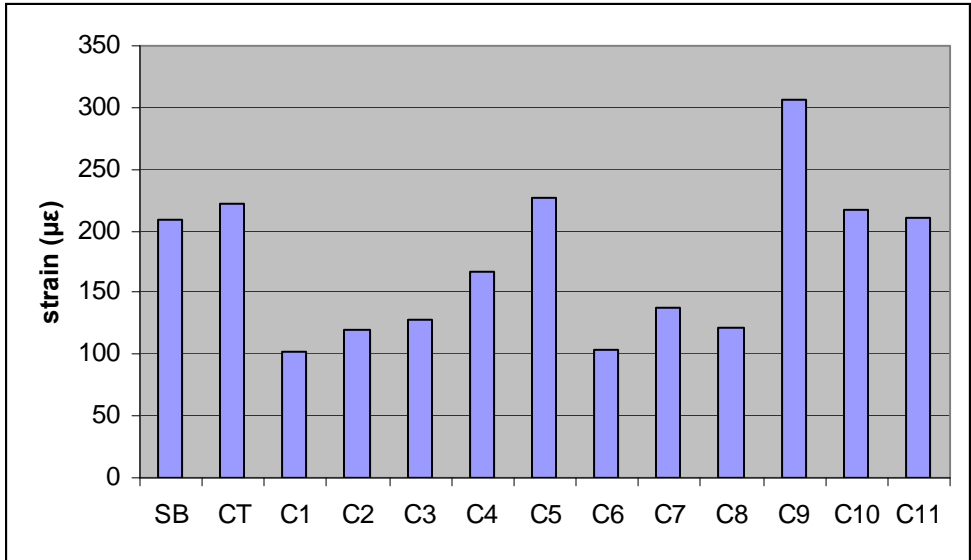


**Figure 38.** Chart showing strain ( $\mu\epsilon$ ) at 700 N for all models and cadavers

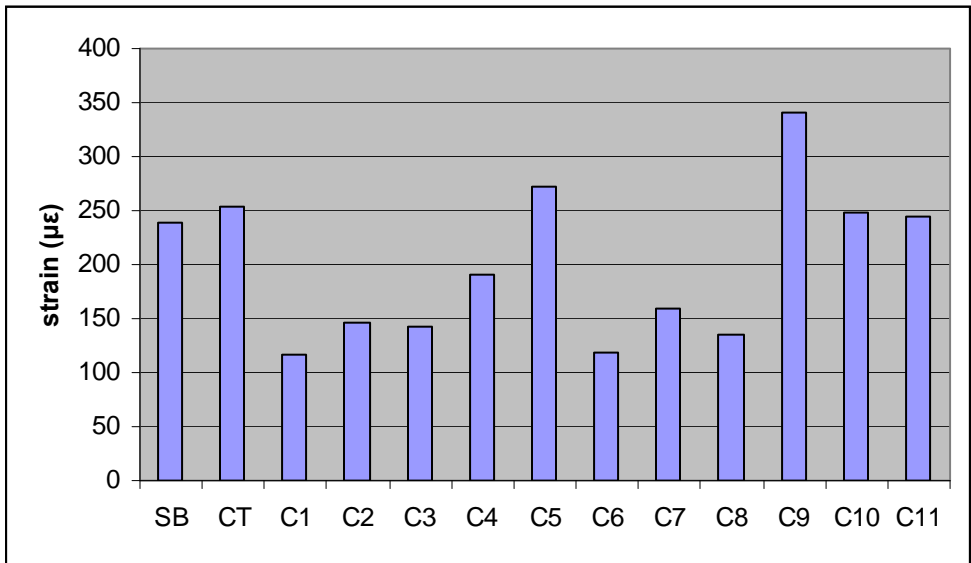


**Figure 39.** Chart showing strain ( $\mu\epsilon$ ) at 800 N for all models and cadavers

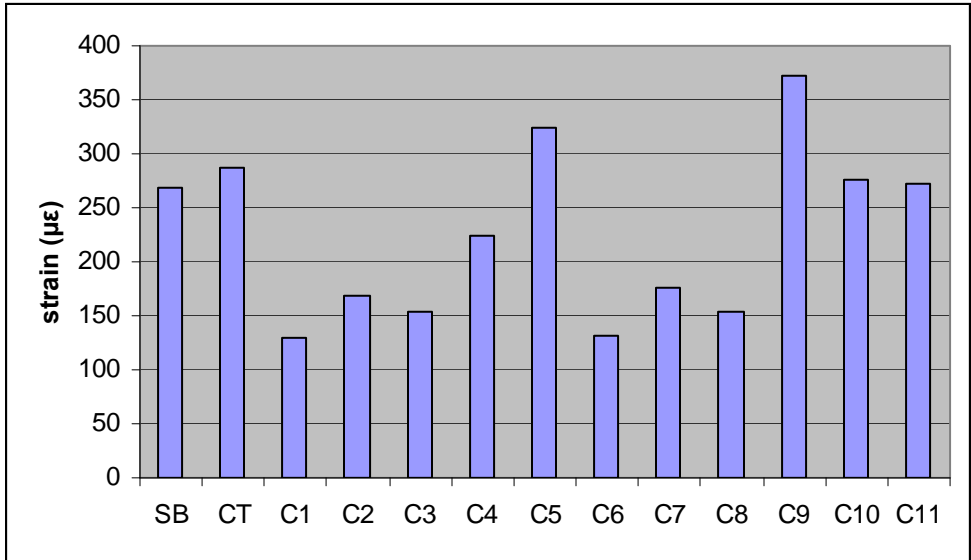


**Figure 40.** Chart showing strain ( $\mu\epsilon$ ) at 900 N for all models and cadavers

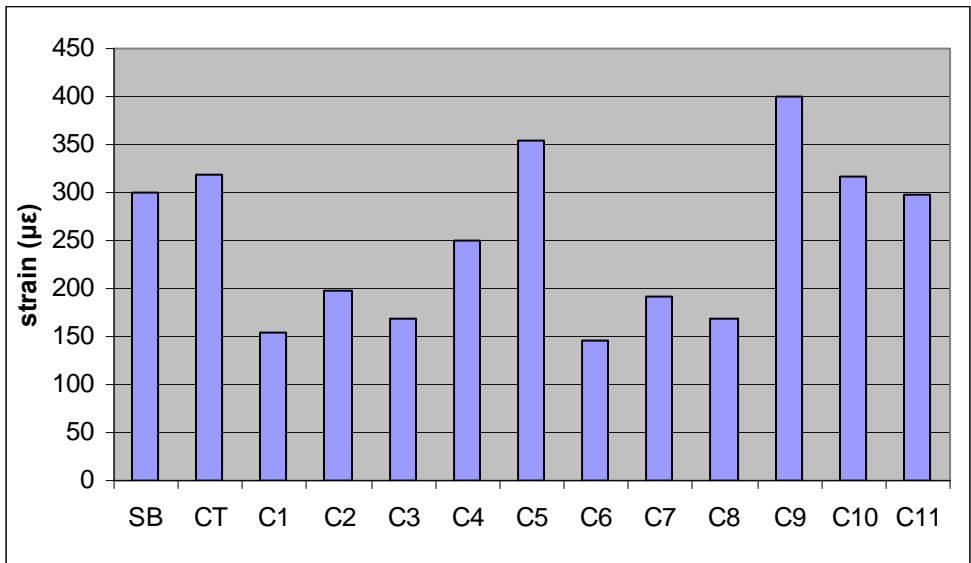


**Figure 41.** Chart showing strain ( $\mu\epsilon$ ) at 1000 N for all models and cadavers

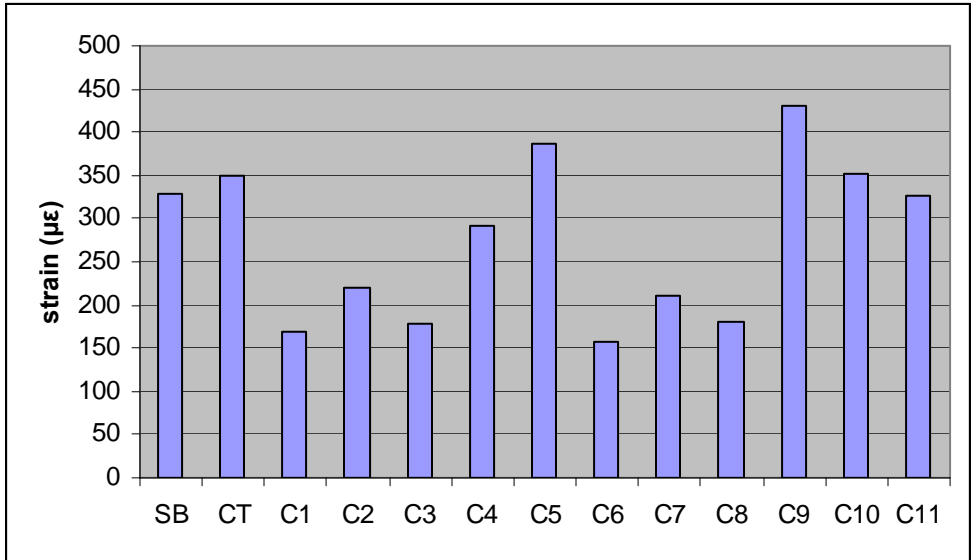


**Figure 42.** Chart showing strain ( $\mu\epsilon$ ) at 1100 N for all models and cadavers

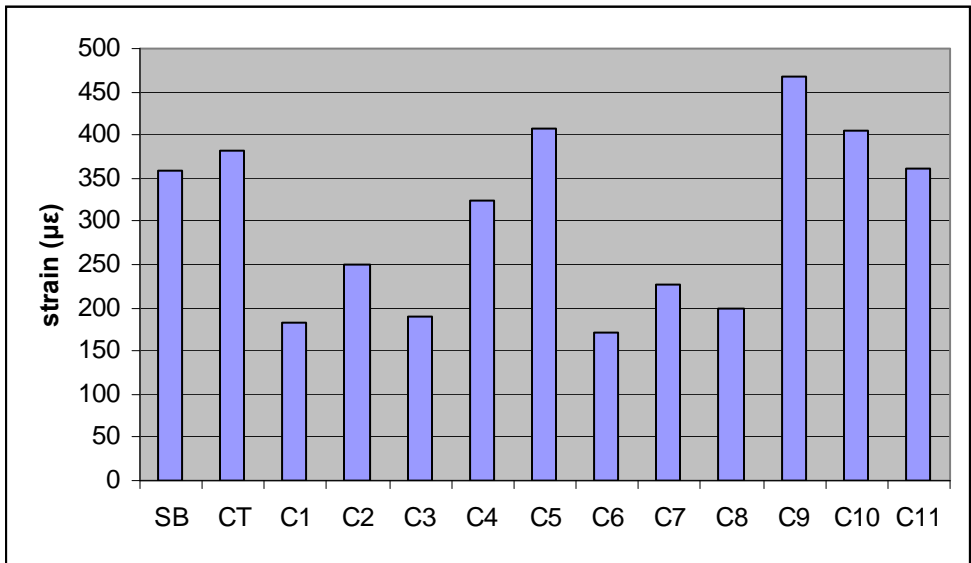


**Figure 43.** Chart showing strain ( $\mu\epsilon$ ) at 1200 N for all models and cadavers

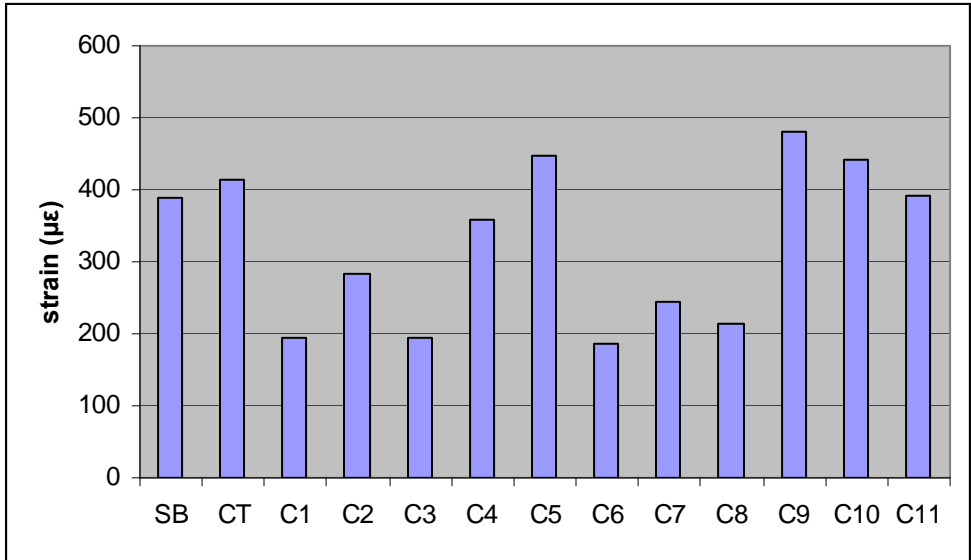


**Figure 44.** Chart showing strain ( $\mu\epsilon$ ) at 1300 N for all models and cadavers

## BIBLIOGRAPHY

- Algietti P, Cuomo P, Ciron F, Boerger T O. Double-Bundle ACL Reconstruction: *Surgical Technique. Operative Techniques in Orthopedics, Anatomic ACL Reconstruction, Part 2: Surgical Concepts*. 2005; 15(2):111-115.
- BEL Repository 2005, [www.biomedtown.org](http://www.biomedtown.org)
- Berg EE. Lateral femoral condyle fracture after endoscopic anterior cruciate ligament reconstruction. *Arthroscopy*. 1994; 10:693-696.
- Boden, BP. Dean, GS. Feagin, JA. Garrett, WE. Mechanisms of anterior cruciate ligament injury. *Orthopedics*. 2000; 23(6):573-278.
- Buoncristiani AM, Tjoumakaris FP, Starman JS, Ferretti M, Fu FH. Anatomic Double-Bundle Anterior Cruciate Ligament Reconstruction. *Arthroscopy: The Journal of Arthroscopic & Related Surgery*. 2006; 22(9):1000-1006
- Christel P, Franceschi JP, Sbihi A, Colombet P, Djian P, Bellier G. Anatomic anterior cruciate ligament reconstruction: The French Experience. *Operative Techniques in Orthopedics, Anatomic ACL Reconstruction, Part 2: Surgical Concepts*. 2005; 15(2):103-110.
- Clatworthy M, Amendola A. The anterior cruciate ligament and osteoarthritis. *Clinics in Sports Medicine*. 1999; 18:173–198.
- Cohen SB, Fu FH. Three-portal technique for anterior cruciate ligament reconstruction: use of a central medial portal. *Arthroscopy*. 2007; 23(3):325-330
- Cowin, SC. Bone Mechanics. Boca Raton, Fla. CRC Press 1989.
- Devore JL. Probability and Statistics for Engineering and the Sciences (seventh edition). Duxbury, The Thomson Corporation, 2004.
- Harner CD. Editorial: Double Bundle or Double Trouble? *Arthroscopy*. 2004; 20(10):1013-1014
- Manktelow AR, Haddad FS, Goddard NJ. Late Femoral Condyle Fracture After Anterior Cruciate Ligament Reconstruction. *Am J Sports Med*. 1998; 26:587-590.

- Milano G, Mulas PD, Zirano F, Piras S, Manunta A, Fabbriani C. Comparison Between Different Femoral Fixation Devices for ACL Reconstruction With Doubled Hamstring Tendon Graft: A Biomechanical Analysis. *Arthroscopy: The Journal of Arthroscopic and Related Surgery*. 2006; 22(6): 660-668
- Morrison JB. The mechanics of the knee joint in relation to normal walking. *Journal of Biomechanics*. 1970; 3:51-61.
- Noah J, Sherman OH, Roberts C. Fracture of the supracondylar femur after anterior cruciate ligament reconstruction using patellar tendon and iliotibial band tenodesis. A case report. *Am. J. of Sports Medicine*. 1992; 20(5):615-618.
- Pilkey WD. Peterson's Stress Concentration Factors (2nd Edition). John Wiley & Sons 1997. Online version available at: [www.knovel.com](http://www.knovel.com)
- Radler C, Wozasek GE, Seotz H, Vecsei V. Distal Femoral Fracture Through the Screw Hole of a Ligament Augmentation Device. *Arthroscopy*. 2000; 16:737-39.
- Reilly, D.T. and A.H. Burstein, The Elastic and Ultimate Properties of Compact Bone Tissue. *Journal of Biomechanics*. 1975; 8: 393-405.
- Rho, J.Y., R.B. Ashman, and C.H. Turner, Young's Modulus of Trabecular and Cortical Bone Material: Ultrasonic and Microtensile Measurements. *Journal of Biomechanics*. 1993; 26(2): 111-119.
- Riley WF, Sturges LD, Morris DH. Statics and Mechanics of Materials (2nd Edition). John Wiley & Sons 2002; pg: 591-606
- Ternes JP, Blasier RB, Alexander AH. Fracture of the femur after anterior cruciate ligament reconstruction with a GORE-TEX prosthetic graft. A case report. *Am. J. of Sports Medicine*. 1993; 21(1):147-149.
- Viceconti M., Casali M., Massari B, Cristofolini L, Bassini S, Toni, A. The 'Standardized femur program'. Proposal for a reference geometry to be used for the creation of finite element models of the femur. *J. Biomechanics*. 1996; 29:1241.
- Viceconti M, L Bellingeri, et al. A comparative study of different methods of automatic mesh generation of human femur. *Medical Engineering & Physics*. 1998; 20: 1-10.
- Wiener DF, Siliski JM. Distal femoral shaft fracture: a complication of endoscopic anterior cruciate ligament reconstruction. A case report. *Am J Sports Medicine*. 1996;24(2):244-7.
- Wilson TC, Rosenblum WJ, Johnson DL. Fracture of the Femoral Tunnel After an Anterior Cruciate Ligament Reconstruction. *Arthroscopy*. 2004; 20: E45-E47.
- Yagi, M., Wong, E.K., Kanamori, A., Debski, R.E., Fu, F.H. and Woo, S.L-Y.: The Biomechanical Analysis of an Anatomical ACL Reconstruction. *Am. J. of Sports Medicine*. 2002; 30(5):660-666.

- Zannoni C., Mantovani R., Viceconti M. Material properties assignment to finite element models of bone structures: a new method. *Med. Engineering & Physics*. 1998; 735-740
- Zantop T, Petersen W, Fu FH. Anatomy of the Anterior Cruciate Ligament. *Operative Techniques in Orthopedics, Anatomic ACL Reconstruction, Part 1:Related Basic and Clinical Science*. 2005; 15(1):20-28.
- Zantop T, Petersen W, Sekiya JK, Musahl V, Fu FH. Anterior cruciate ligament anatomy and function relating to anatomical reconstruction. *Knee Surg Sports Traumatol Arthrosc*. 2006; 14: 982–992
- Zantop T, Kubo S, Petersen W, Musahl V, Fu FH. Current Techniques in Anatomic Anterior Cruciate Ligament Reconstruction. *Arthroscopy: The Journal of Arthroscopic & Related Surgery*. 2007; 23(9): 938-947
- Zelle BA, Brucker PU, Feng MT, Fu FH. Anatomical Double-Bundle Anterior Cruciate Ligament Reconstruction. *Sports Medicine*. 2006; 36(2): 99-108.